https://doi.org/10.5194/gmd-2022-153
Preprint. Discussion started: 1 July 2022

Geoscientific Model Development Discussions
Open Access
EGU

SCIATRAN software package (V4.6): update and further development of aerosol, clouds, surface reflectance databases and models

Linlu Mei[a,*], Vladimir Rozanov[a], Alexei Rozanov[a], John P. Burrows[a]

[a]*Institute of Environmental Physics, University of Bremen, Germany*

Abstract

Since the initiation of the development at the Institute of Environmental Physics (IUP), University of Bremen in 1994, the radiative transfer model SCIATRAN (formerly GOMETRAN) has been continuously improved and new versions have been released (Rozanov et al., 1997, 2002, 2005, 2014, 2017). In the course of development, the SCIATRAN software package became capable to simulate radiative transfer processes through an atmosphere-ocean system with a variety of approaches to treat the sphericity of the atmosphere (plane-parallel, pseudo-spherical, approximate spherical and full spherical solutions) in both scalar and vector modes. Supported by a variety of build-in databases and parameterizations, these capabilities made SCIATRAN widely used for various remote sensing applications related to the retrieval of atmospheric trace gases and characteristics of aerosols, clouds and surface. This paper presents an overview of the clouds, aerosol and surface (CAS) databases and models implemented in the SCIATRAN software package (V4.6) and provides some recommendations on their usage. The new implementations offer potential users flexible interface to perform radiative transfer simulations: 1) in the case of multi-layer liquid water, ice and mix-phase clouds; 2) employing typical aerosol type parameterizations (including vertical variability) used in satellite and model communities as well as updated databases; 3) including various surface BRDF and albedo

*Corresponding author
Email address: mei@iup.physik.uni-bremen.de (Linlu Mei)

https://doi.org/10.5194/gmd-2022-153
Preprint. Discussion started: 1 July 2022

Geoscientific Model Development Discussions

models for land, vegetation, ocean, snow and melt ponds on sea ice.

The most recent SCIATRAN version is freely available for students and scientists affiliated at academic facilities after a registration at the website of IUP, University of Bremen: http://www.iup.physik.uni-bremen.de/sciatran.

Keywords: `SCIATRAN, Aerosol, Clouds, Surface reflectance`

1. Introduction

Shortly after the beginning of space age in 1957, the first earth observation satellite flew around the Earth and discovered the Van Allen radiation belts. Since then, Earth observations satellites have been evolving and a global observation system utilising remote sensing instrumentation is now being developed. The satellite instruments have been continually evolving in the past decades. However, the explosion in the exploration of earth observation data would not have been possible without i) the simultaneous and remarkable increase in the speed of computers and their data storage and ii) the development of sofisticated forward radiative transfer models (RTMs) and retrieval algorithms.

Increasingly accurate RTMs have been developed to meet the need to simulate earth observation data from the evolving observing system. SCIATRAN, which is the subject of this paper, is a comprehensive radiative transfer software package. SCIATRAN can simulate radiative transfer processes including polarization through earth's atmosphere-ocean-land-cryosphere system in the spectral range from 175 nm to 40 μm under any observation/illumination geometries (Rozanov et al., 2014).

Since SCIATRAN was released for the use by scientists and students for research in a non-commercial application, it has become a well-used model. Fig. 1 shows the global distribution of SCIATRAN users up to December 2021. One can see that SCIATRAN software has more than 950 external users from 301 cities in 58 countries. About in 1400 publications (from google scholar) have used the SCIATRAN software package in different studies. The topics of re-

https://doi.org/10.5194/gmd-2022-153
Preprint. Discussion started: 1 July 2022

Geoscientific Model Development Discussions
Open Access
EGU

search addressed by publications using SCIATRAN are shown in Fig. 2. This plot shows the bibliometric network of SCIATRAN since 1994 (till December 2021), and the scientific topics investigated using SCIATRAN software package are presented. Topics such as retrieval of atmospheric and surface parameters using satellite data are the most important application areas for the SCIATRAN user community.

Continuous developments of SCIATRAN software include two aspects: i) implementation of new features in the radiative transfer and retrieval modules; ii) update and implementation of databases and new surface reflectance models. This paper focuses on the update of cloud & aerosol databases and implementation of new surface Bidirectional Reflectance Distribution Function (BRDF) models in the most recent SCIATRAN version - V4.6. A comprehensive overview of the existing Cloud, Aerosol and Surface (CAS) databases and models was presented by Rozanov et al. (2014). However, a major extension of the CAS

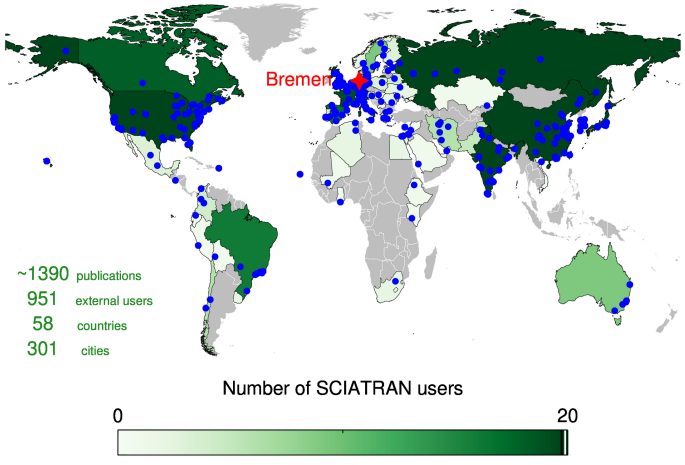

Figure 1: Geograpic distribution of SCIATRAN users worldwide till Dec. 2021. The color indicate the total number of user for selected country and the blue dot is the city where SCIATRAN users located in given country. The red star indicates city Bremen.

https://doi.org/10.5194/gmd-2022-153
Preprint. Discussion started: 1 July 2022

Geoscientific Model Development
Discussions
Open Access
EGU

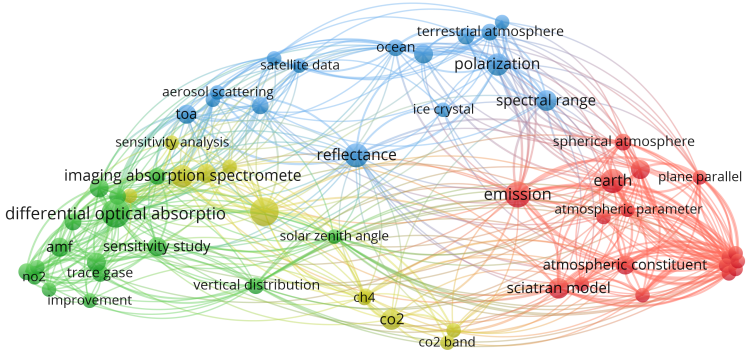

Figure 2: The bibliometric network of SCIATRAN since 1994 created by VOSviewer

databases and models in SCIATRAN has been done after 2014. To bring the user community up to date with the options available within SCIATRAN, this paper describes the improved cloud and aerosol databases and the usage of new surface BRDF models, available in SCIATRAN.

65

https://doi.org/10.5194/gmd-2022-153
Preprint. Discussion started: 1 July 2022


Geoscientific Model Development Discussions
Open Access
EGU

The paper is structured as follows. Sect. 2 contains brief information about general capabilities of the SCIATRAN software. Sect. 3 presents brief summary of the new features in SCIATRAN V4.6. In Sect. 4 we summarize new CAS databases and models implemented in SCIATRAN. Sect. 5 describes the optical properties of selected CAS. Sect. 6 shows some examples/comparisons of forward simulations using the new implementations. The conclusions are presented in Sect. 7.

2. General capabilities of SCIATRAN software

This section gives an overview of the main features and general capabilities of the SCIATRAN software for potential users.

In SCIATRAN, polarized (vector) and scalar radiative transfer calculations can be performed in plane-parallel, pseudo-spherical, approximate spherical or fully spherical geometry. Vertical inhomogeneities for parameters such as temperature, pressure profiles, gaseous absorber concentration, aerosol particles number density, and multi-layer liquid water and ice clouds can be easily accounted for. For inexperienced users, an option of a vertically homogeneous atmospheric layer, which requires minimum number of input parameters, might be useful.

The surface reflection can be described as 1) wavelength dependent Lambertian reflection or constant albedo; 2) BRDF including parameterizations for a variety of surface types (ocean, vegetation, soil, snow, melt ponds and sea ice). In particular, in the case of light reflection by ocean surface, the SCIATRAN software enables to consider the Fresnel reflection from absolutely calm and wind-roughed surface (accounting for polarization), whitecap reflection, and water leaving radiation. Reflection by white ice and melt ponds on sea ice can also be accounted for. In addition, a coupled ocean-ice-atmosphere system can be considered to simulate the radiative transfer over and under the ice/water surface.

The software package has been designed to perform fast and accurate simulations of radiance spectra appropriate to atmospheric remote sensing observations

https://doi.org/10.5194/gmd-2022-153
Preprint. Discussion started: 1 July 2022


Geoscientific Model Development Discussions
Open Access
EGU

in the UV-VIS-NIR-SWIR-TIR spectral ranges. In particular, the calculations can be performed in the spectral range from 175.44 nm to 40 μm, including O_2 Schumann-Runge and Herzberg absorption bands in UV spectral range, various gaseous absorbers such as O_3, NO_2, CIO, OCIO, BrO, HCHO, SO_2, NO_3, O_4, O_2, H_2O, CO_2, CO, CH_4, N_2O, and thermal emission in the TIR spectral range. All relevant elastic scattering processes such as Rayleigh scattering, aerosol and cloud scattering & absorption can be taken into account. Additionally, important inelastic scattering processes such as rotational Raman scattering in the atmosphere (including electron spin-rotational splitting) (Rozanov and Vountas, 2013, Lelli et al., 2017, Rozanov et al., 2021), vibrational Raman scattering (Rozanov et al., 2017), and Colored Dissolved Organic Matter (CDOM) fluorescence (Wolanin et al., 2015) in the ocean can be accounted for. SCIATRAN also includes a retrieval block, which enables a continually increasing number of earth observation data products from ground based, ship, aircraft or satellite borne sensors to be delivered in near real-time. This block, however, is not a part of the freely distributed software package.

Employing the SCIATRAN software, users can calculate radiance/intensity (scalar mode) or Stokes vector (vector mode), weighting functions (Jacobian matrix) for scalar and vector case, air mass factors (AMF), slant columns, vertically resolved AMFs (box AMFs), fluxes (actinic, upwelling, downwelling, diffuse and total), spherical albedo, diffuse transmission, vertical optical depth. Such characteristics of radiation field as fluxes, spherical albedo, and diffuse transmission can also be calculated assuming specific isotropic illumination conditions of a medium from above and below.

The SCIATRAN software contains not only different solvers which are capable to perform radiative transfer calculations through plane-parallel or spherical atmosphere but also numerous parameterizations of Rayleigh scattering, databases of aerosol and cloud optical properties as well as various models of bidirectional surface reflection, which significantly facilitate the usage of software especially for novice users. Taking into account that parameterizations of Rayleigh scattering have been discussed in (Rozanov et al., 2014), following sections will present

https://doi.org/10.5194/gmd-2022-153
Preprint. Discussion started: 1 July 2022


Geoscientific Model Development Discussions

new implemented databases of aerosol and cloud optical properties as well as models of bidirectional surface reflection. The consideration of databases for numerous gaseous absorber including HITRAN 2020 molecular spectroscopic database is out of scope of this paper.

3. Overview of new SCIATRAN features

While the initial development of SCIATRAN was dedicated to the satellite missions GOME (Global Ozone Monitoring Experiment) and SCIAMACHY (SCanning Imaging Absorption spectroMeter for Atmospheric CHartography) and their products (Burrows et al., 1995, Bovensmann et al., 2010, Buchwitz et al., 2013, Richter et al., 2005, Noël et al., 2018, Arosio et al., 2018, Weber et al., 2018), the implementation of CAS databases and models in SCIATRAN is mainly driven by the developments of the eXtensible Bremen Aerosol/cloud and surfacE parameters Retrieval (XBAER) algorithm and its products. The XBAER algorithm is now capable to provide global data products for clouds (Mei et al., 2017b, 2018a, 2019), aerosol (Mei et al., 2017a, 2018b, 2020a,b) and surface parameters (Mei et al., 2021a,b). The further developments of SCIATRAN support 1) the design of new instruments (e.g., Carbon Monitoring Satellite (CarbonSat) (Buchwitz et al., 2013), Methane Airborne MAPper (MAMAP) (Gerilowski et al., 2011)); 2) the release of new versions of atmospheric and surface satellite products in Institute of Environmental Physics (IUP), University of Bremen; 3) the explore of new applications for related research topics worldwide.

Table 1 summarizes new implementations of CAS since the paper of Rozanov et al. (2014). In particular, optical characteristics of liquid water cloud database have been extended to cover the water droplet effective radii between 2 - 40 μm in contrast to 4 - 20 μm in the previous version. The Baum (Baum et al., 2011) and Yang (Yang et al., 2013) ice crystal databases have been included in SCIATRAN. Many important details of Yang database implementation can be found

https://doi.org/10.5194/gmd-2022-153
Preprint. Discussion started: 1 July 2022

Geoscientific Model Development Discussions
Open Access
EGU

Table 1: Databases and models described in (Rozanov et al., 2014) and in this paper

Topic	Rozanov et al. (2014)	This paper
Cloud	liquid water and ice clouds	update of liquid water and ice clouds
Aerosol	OPAC 3, WMO, LOWTRAN	OPAC 4, MERRA, XBAER, MODIS Dark-Target, spheroidal dust
Surface	RPV, modified RPV (mRPV) mRPV plus facet, RTLSR	XBAER, FASMAR, RTLSRS, snow and melt ponds on sea ice

in Pohl et al. (2020).

Aerosol type parameterizations such as Moderate Resolution Imaging Spectroradiometer (MODIS) Dark-Target (DT) over Land (Levy et al., 2013), and ocean (Remer et al., 2005), Modern-Era Retrospective analysis for Research and Applications (MERRA) (Randles et al., 2017), and XBAER (Mei et al., 2017a) have been implemented. Moreover, the updated Optical Properties of Aerosols and Clouds (OPAC) dataset (Köpke et al., 2015) and optical parameters of dust aerosol particles according to Dubovik et al. (2006) have also been included.

The XBAER surface reflectance parameterization (Mei et al., 2017a), RossThick-LiSparseReciprocal-Snow (RTLSRS) (Jiao et al., 2019), Fast and Accurate Semi-analysical Model of Atmosphere-surface Reflectance (FASMAR) (Mei et al., 2022), and BRDF models for snow, white ice and melt ponds on sea ice are now available.

In recent years, to address the exponentially increasing amount of remote sensing data, fast radiative transfer models focused on specific data products have been developed. Examples are i) FASMAR (Fast and Accurate Semi-analytical Model of Atmosphere and Surface Reflectance (Mei et al., 2022) is used with XBAER to retrieve surface (e.g., snow grain size, specific surface area) and aerosol products (e.g., AOT); ii) FOCAL: Fast atmOspheric traCe gAs retrievaL (Reuter et al., 2017) uses a simplified RTM to determine the dry mole fractions of carbon dioxide, XCO2, and methane, XCH4, from measurements of the radiance in the Near Infrared, NIR, and Short-wave Infrared, SWIR. These

https://doi.org/10.5194/gmd-2022-153
Preprint. Discussion started: 1 July 2022


Geoscientific Model Development Discussions
Open Access
EGU

have benefited also from SCIATRAN, in its being a high accuracy reference RTM.

4. CAS databases and models implemented in SCIATRAN

In this section, we briefly introduce the CAS databases and models newly implemented in SCIATRAN. All databases can be used to perform radiative transfer simulations in the spectral range at least between 225 nm and 2.5 μm.

4.1. Aerosol

In our seminal paper (Rozanov et al., 2014) dedicated to the software package SCIATRAN such aerosol models and databases as World Meteorological Organization (WMO) (Bolle, 1986), LOWTRAN (Levoni et al., 1997) and OPAC version 3 (Hess et al., 1998) have been described. We recall that WMO and LOWTRAN databases contain optical characteristics of different aerosol components and aerosol types, respectively. In particular, in the WMO database six aerosol components are included, namely water soluble, dust, oceanic, soot, stratospheric and volcanic. The commonly used aerosol types (e.g. continental, maritime, urban) are defined by the external mixture of the optical properties those six components. The user has to specify the vertical profile of the aerosol extinction coefficient at a reference wavelength.

The LOWTRAN database (version 7) consists of 1) pre-defined extinction and scattering coefficients; 2) asymmetry parameters of aerosol types located at different atmospheric layers (i.e. boundary layer, troposphere, stratosphere and mesosphere). The basic aerosol types in boundary layer include rural, urban and maritime aerosols. Only one type is available for the tropospheric aerosols. For both boundary layer and the troposphere, the humidity and visibility is to

https://doi.org/10.5194/gmd-2022-153
Preprint. Discussion started: 1 July 2022


Geoscientific Model Development Discussions
Open Access
EGU

be selected by the users. In the stratosphere, the users can select 1) aerosol loading for the background and volcanic (moderate, high, extreme) conditions; 2) aerosol types of fresh and aged volcanic aerosols. For the mesosphere a choice between normal aerosol state and a transition from the volcanic stratosphere to the normal mesosphere is available.

The OPAC (version 3) database implemented into the SCIATRAN software consists of refractive indices and parameters of log-normal particle size distribution functions of predefined components such as insoluble, meteoritic dust, mineral (nuc., acc., coa., mode), mineral-transported, soot, sulfate, sea salt (acc., coa. mode), and water soluble. The optical properties of an aerosol type are calculated as the external mixture of predefined aerosol components in OPAC using the Mie code published by Mishchenko et al. (1999), which is incorporated in SCIATRAN.

The following new aerosol databases have been implemented in the recent SCIATRAN version: an updated OPAC database, MODIS Dark-Target (both land and ocean), MERRA, XBAER, and Dust aerosol types. These aerosol types provide aerosol paramterization methods, which are well-received by the aerosol community.

When selecting a suitable aerosol database or parameterization, beside the requirement with respect to appropriate spectral range, the possibility to use altitude dependent particle number density and optical properties (extinction cross-section, Single Scattering Albedo (SSA) and phase function) is also an important issue. In contrast to the aerosol particle number density, which can be defined as a function of altitude, for all newly implemented aerosol types in SCIATRAN, altitude dependent particle optical properties can only be defined when using MERRA or OPAC aerosol types. It is worth noticing that the usage of MERRA types is significantly simpler as compared to OPAC, because it does not require from user any a priori knowledge about chemical composition and micro-physical properties of aerosol types in different atmospheric layers. The aerosol types which were available in previous SCIATRAN version (e.g. WMO and LOWTRAN) enable the users to describe the altitude dependent optical

https://doi.org/10.5194/gmd-2022-153
Preprint. Discussion started: 1 July 2022


Geoscientific Model Development Discussions
Open Access
EGU

properties only for pre-defined altitude layers (boundary layer, troposphere, stratosphere, and mesosphere). The newly implemented MODIS Dark-Target, XBAER, and Dust aerosol parameterizations define altitude independent aerosol types.

4.1.1. OPAC aerosol type

In the previous version of SCIATRAN paper (Rozanov et al., 2014), the details of OPAC version 3 database has been described. A new version of OPAC (version 4.0) was released recently by Köpke et al. (2015). The main improvement is the update of shape of mineral dust, from spherical to prolate spheroids. The usage of a spherical assumption for dust particles was proven to introduce large error for both aerosol properties retrieval (Zhao et al., 2003) and dust radiative forcing calculations (Mishchenko, 2001). The usage of this aerosol type within the SCIATRAN software does not require the Mie calculations because the database in this case includes the phase function at discrete number of scattering angles and extinction and scattering coefficients pre-calculated employing T-matrix and geometric optics methods (Köpke et al., 2015).

4.1.2. MODIS Dark-Target aerosol types

The MODIS-DT aerosol type is operationally used to derive NASA aerosol properties dataset from MODIS and Virible Infrared Imaging Radiometer Suite (VIIRS) instruments (Levy et al., 2013, Remer et al., 2020). This aerosol type provides an aerosol paramterization method, which is well-received by the aerosol community.

The MODIS dark-target aerosol type parameterization is different for aerosols over the land and ocean.

Dark-Target aerosol type over land (MODIS-DT).

The MODIS-DT aerosol parameterization implemented into the SCIATRAN

https://doi.org/10.5194/gmd-2022-153
Preprint. Discussion started: 1 July 2022


Geoscientific Model Development Discussions
Open Access
EGU

software offers the following aerosol types: Weakly Absorbing (WA), Moderately Absorbing (MA), Strongly Absorbing (SA), and specific spheroidal (dust). Although the continental aerosol type was also included in the original MODIS Dark-Target over land aerosol parameterization, this type is not included in the current SCIATRAN database because this type is not used in the XBAER algorithm according to our investigation for MERIS instrument.

Each aerosol type contains fine and coarse modes (hereafter mode 1 and 2), which are characterized by the volume PSD given by

$$\frac{dV}{d\ln r} = \frac{V_0}{\sqrt{2\pi}\,\sigma}\exp\left[-\frac{(\ln r - \ln r_v)^2}{2\sigma^2}\right], \tag{1}$$

where V_0 is the total volume, r_v is the mode radius and σ is the standard deviation. Parameters of the aerosol Particle Size Distribution (PSD) function and the Refractive Index (RI) for each mode are represented as functions of the Aerosol Optical Thickness (AOT) at the wavelength of 0.55 μm. The parameterization formulas for each aerosol type and mode are listed in Table 2. We note that the relationships presented in the table are valid for $\tau \leq 2$ for MA and SA types and for $\tau \leq 1$ for WA and dust types. For larger values of τ, $\tau = 2$ and $\tau = 1$, respectively, is to be used in the formulas.

For selected aerosol type and AOT, SCIATRAN calculates parameters of the volume PSD and RI for fine and coarse modes according to Table 2. Then, employing incorporated Mie code, the scattering and absorption cross-sections as well as the scattering matrix are calculated. The optical parameters for the selected aerosol type are calculated thereafter as follows

$$\sigma_p = f\,\sigma_{p_1} + (1-f)\,\sigma_{p_2}\ , \tag{2}$$

where subscript "p" denotes scattering "s", absorption "a" or extinction "e" cross-section and f is the fraction of fine mode given by $f = N_{01}/(N_{01}+N_{02})$. To calculate the fine mode fraction, the following relationship between the total volume, V_0, and the total particle number density, N_0, is employed

$$N_0 = V_0\,\frac{3}{4\pi r_v^3}\exp\left(\frac{9\sigma^2}{2}\right)\ . \tag{3}$$

https://doi.org/10.5194/gmd-2022-153
Preprint. Discussion started: 1 July 2022

Geoscientific Model Development Discussions
Open Access
EGU

Table 2: Parameters of PSD function and refractive indices of DT-land aerosol types according to Levy et al. (2007).

Type	Mode	r_v (μm)	σ	V_0 ($\mu m^3/\mu m^2$)	Refractive Index
Moderately	1	$0.0203\tau+0.145$	$0.1365\tau+0.3738$	$0.1642\tau^{0.7747}$	1.43-(-0.002τ+0.008) i
absorbing	2	$0.3364\tau+3.101$	$0.098\tau+0.7292$	$0.1482\tau^{0.6846}$	1.43-(-0.002τ+0.008) i
Weakly	1	$0.0434\tau+0.1604$	$0.1529\tau+0.3642$	$0.1718\tau^{0.8213}$	1.42-(-0.0015τ+0.007) i
absorbing	2	$0.1411\tau+3.3252$	$0.1638\tau+0.7595$	$0.0934\tau^{0.6394}$	1.42-(-0.0015τ+0.007) i
Strongly	1	$0.0096\tau+0.1335$	$0.0794\tau+0.3834$	$0.1748\tau^{0.8914}$	1.51-0.02 i
absorbing	2	$0.9489\tau+3.4479$	$0.0409\tau+0.7433$	$0.103\tau^{0.6824}$	1.51-0.02 i
Spheroidal	1	$0.1416\tau^{-0.0519}$	$0.7561\tau^{0.148}$	$0.0871\tau^{1.026}$	$1.48\,\tau^{-0.021}$ - $0.0025\tau^{0.132}$ i (0.47)
(dust)					$1.48\,\tau^{-0.021}$ - 0.002 i (0.55)
					$1.48\,\tau^{-0.021}$ - $0.0018\tau^{-0.08}$ i (0.66)
					$1.46\,\tau^{-0.040}$ - $0.0018\tau^{-0.30}$ i (2.1)
	2	2.2	$0.554\tau^{-0.0519}$	$0.6786\tau^{1.0569}$	the same as for Mode 1

The phase function is calculated as

$$p(\gamma) = \frac{\sigma_{s_1}\, p_1(\gamma) + \sigma_{s_2}\, p_2(\gamma)}{\sigma_s}\,, \tag{4}$$

where γ is the scattering angle.

The usage of MODIS-DT aerosol type parameterization within SCIATRAN software requires the user to select one of the above discussed aerosol types and to provide AOT at the wavelength of 0.55 μm. In addition, the user can define any shape, $S_h(z)$, of the aerosol number density vertical distribution. The number density profile is then calculated as

$$N(z) = \frac{\tau}{\sigma_e \int\limits_0^H S_h(z)\, dz}\, S_h(z)\,, \tag{5}$$

where H is the top height of the aerosol layer. In the operational MODIS-DT aerosol product, the aerosol layer is assumed to be located between 0 - 3 km with an exponential number density vertical distribution.

MODIS-DT aerosol types were used in the framework of SCIATRAN software to calculate the lookup tables widely used in the AOT retrieval algorithm over

https://doi.org/10.5194/gmd-2022-153
Preprint. Discussion started: 1 July 2022


Geoscientific Model Development Discussions
Open Access
EGU

land (Mei et al., 2017a, 2020b).

Dark-Target aerosol type over ocean (MODIS-OC).

Unlike the land case, the aerosol type over the ocean in the DT algorithm is defined by selecting one of the four fine modes (F1, F2, F3, F4) and one of the five coarse modes (C1, C2, C3, C4, C5). The PSD parameters and RI are given in Table 3. For wavelegths selected by users, the Mie code is used by the SCIATRAN software to calculate scattering and extinction cross-sections as well as scattering matrices. The fine mode, coarse mode, and the fraction of coarse mode are input parameters. In contrast to the MODIS-DT aerosol type, which requires AOT as an input parameter, a vertical profile of the aerosol particles number density in physical units needs to be provided over ocean. Using the calculated extinction cross-section and number density profile, AOT will be calculated and written out by the SCIATRAN software.

4.1.3. XBAER aerosol type over ocean (XBAER-OC)

The XBAER aerosol type was originally designed for the usage within the framework of the XBAER retrieval algorithm. A similar strategy, as described by Levy et al. (2007), has been employed to obtain aerosol types over the ocean. In particular, the statistical analysis was performed using the Maritime Aerosol Network (MAN) observations (Smirnov et al., 2009) and four aerosol types, namely pure maritime, pollution 1, pollution 2 and dust influenced were defined. Table 4 shows the volume PSD parameters and RI of these predefined aerosol types as used in the XBAER algorithm over ocean and implemented into the SCIATRAN software.

A slight difference as compared to the MODIS-DT aerosol types is that the XBAER ocean aerosol type is parameterized not only with respect to AOT at $0.55\,\mu$m, τ, but also with respect to fine-mode AOT at $0.55\,\mu$m, τ_f. τ_f is de-

https://doi.org/10.5194/gmd-2022-153
Preprint. Discussion started: 1 July 2022

Geoscientific Model Development Discussions

Table 3: Parameters of PSD function and refractive indices of DT-ocean aerosol fine and coarse modes according to Remer et al. (2005). Details of the table below can be found on https://darktarget.gsfc.nasa.gov/algorithm/ocean/aerosol-models

Mode	r_g	σ	RI(0.466 - 0.857μm)	RI(1.241μm)	RI(1.628μm)	RI(2.113μm)
F1	0.07	0.4	1.45-0.0035i	1.45-0.0035i	1.45-0.01i	1.40-0.005i
F2	0.06	0.6	1.45-0.0035i	1.45-0.0035i	1.45-0.01i	1.40-0.005i
F3	0.08	0.6	1.40-0.0020i	1.40-0.0020i	1.39-0.005i	1.36-0.003i
F4	0.10	0.6	1.40-0.0020i	1.40-0.0020i	1.39-0.005i	1.36-0.003i
C1	0.40	0.6	1.35-0.001i	1.35-0.001i	1.35-0.001i	1.35-0.001i
C2	0.60	0.6	1.35-0.001i	1.35-0.001i	1.35-0.001i	1.35-0.001i
C3	0.80	0.6	1.35-0.001i	1.35-0.001i	1.35-0.001i	1.35-0.001i
C4	0.60	0.6	1.53-0.003 i (0.47) 1.53-0.001i (0.55) 1.53-0.000i (0.65) 1.53-0.000i (0.86)	1.46-0.000i	1.46-0.001i	1.46-0.000i
C5	0.50	0.8	the same as for Mode C4	1.46-0.000i	1.46-0.001i	1.46-0.000i

fined as the product of total AOT at 0.55 μm and fine mode volume fraction, which is also a function of τ. The fine mode volume fraction is calculated as $f_v = V_{01}/(V_{01} + V_{02})$, where V_{01} and V_{02} are given in Table 4 as function of τ for mode 1 and 2, respectively.

The input parameters for this parameterization are the aerosol type (pure maritime, pollution 1, pollution 2 or dust influenced), AOT at 0.55 μm, and the shape of aerosol number density profile similarly to MODIS-DT aerosol type over land.

The combination of MODIS-DT for land and XBAER-OC for ocean aerosol types enable the same treatment of global aerosol prameterization in the XBAER algorithm. For a given location and time, a unique aerosol type can be selected and used for global aerosol retrieval over land and ocean (Mei et al., 2017a, 2018a). The XBAER aerosol type is operationally used to derive ESA Climate Change Initiative (CCI) and Copernicus Climate Change Service (C3S) aerosol properties dataset from MEdium Resolution Imaging Spectrometer (MERIS)

https://doi.org/10.5194/gmd-2022-153
Preprint. Discussion started: 1 July 2022

Geoscientific Model Development Discussions

Table 4: Parameters of PSD function and refractive index of XBAER-ocean aerosol types according to Mei et al. (2018b).

Type	Mode	r_v (μm)	σ	V_0 ($\mu m^3/\mu m^2$)	Refractive Index
Pure Maritime	1	$0.115\tau_f{}^{-0.05}$	$0.42\tau_f{}^{-0.02}$	0.078τ	1.415-0.002i
	2	$1.376\tau_f{}^{-0.06}$	$0.732\tau_f{}^{0.016}$	0.588τ+0.002	1.363-3 10^{-9} i
Pollution 1	1	0.042τ+0.137	$0.435\tau_f{}^{0.076}$	0.144τ+0.009	1.48+0.053τ-(-0.002τ+0.006)i
(Organic/black carbon)	2	1.122τ+1.528	$0.658\tau_f{}^{-0.05}$	$0.059\tau^{-0.18}$	1.48+0.053τ-(-0.002τ+0.006)i
Pollution 2	1	0.053τ+0.144	$0.499\tau^{0.092}$	0.141τ+0.015	1.419+0.037τ-(-0.002τ+0.005)i
(Sulfates)	2	0.31τ+2.195	$0.6\tau^{-0.06}$	0.115τ+0.018	1.419+0.037τ-(-0.002τ+0.005)i
Dust influenced	1	0.048τ+0.117	$0.556\tau_f{}^{-0.03}$	0.035τ+0.01	$0.0025\tau^{0.132}$
(dust)	2	$0.072\tau_f$+1.622	$0.531\tau^{-0.08}$	$0.617\tau^{1.15}$	$0.0025\tau^{0.132}$

and Ocean and Land Colour Instrument (OLCI) instruments using lookup table calculated with SCIATRAN software (Mei et al., 2017a, 2018b).

4.1.4. Dust aerosol type

Dust aerosol is a very important aerosol type. Many investigations has been done specifically for the dust aerosol. For example, compared to OPAC version 3.0, the OPAC version 4.0 mainly improves the treatment of the dust. In the MODIS-DT aerosol type, the spheroidal dust can also be used. However, the online calculation of the aerosol optical parameters in the case of non-spherical particles is usually very time consuming. To reduce the calculation time, the pre-calculated kernel look-up-tables and software to calculate optical parameters of dust aerosol type were presented by Dubovik et al. (2006). This software package is not yet included in SCIATRAN, but SCIATRAN is capable to read optical parameters of dust aerosol calculated externally employing the kernels look-up-table. Thus, the input parameters for this aerosol type are pre-calculated optical parameters, AOT at selected wavelengths, and the aerosol number density profile.

The Dubovik dust aerosol type is operationally used to derive ESA Climate Change Initiative (CCI) aerosol properties dataset from Polarization and Anisotropy of Reflectances for Atmospheric science coupled with Observations from a Lidar

https://doi.org/10.5194/gmd-2022-153
Preprint. Discussion started: 1 July 2022

(PARASOL) (Dubovik et al., 2014).

This aerosol type was also used to calculate with SCIATRAN software the TOA reflectance of aerosol contaminated clouds and to support the derivation of AOT above cloud over western Africa (Mei et al., 2019). Moreover, the possibilities of combination the dust aerosol type with other aerosol types (e.g. WMO type) implemented in SCIATRAN was successfully demonstrated by Mei et al. (2019). The full release of this new implementation will be included in the upcoming SCIATRAN version.

4.1.5. MERRA aerosol type

A gap between the satellite-derived and model-simulated aerosol properties exists due to different treatments of aerosol types in satellite and model communities. In fact, aerosol type and corresponding optical properties in model community typically depend on time, geographic location, and altitude, whereas the dependence of aerosol type on the altitude is not accounted for in satellite community. To minimize this gap, we decided to propose a new global aerosol type parameterization for the XBAER algorithm. The new aerosol type parameterization uses the aerosol optical properties from the MERRA aerosol components. As the first stage these MERRA aerosol components are included in the SCIATRAN software.

The MERRA model contains 15 aerosol tracers (components): sulfate (SU), hydrophobic and hydrophilic modes of organic carbon (OC) and black carbon (BC) aerosol, and five non-interacting size bins for dust (DU) and sea salt (SS) aerosol (see Table 5). The optical database for each tracer, i, includes extinction, Q_{ei}, and scattering, Q_{si}, efficiency and expansion coefficients of scattering matrix elements pre-calculated at predefined wavelengths and humidity grids. Additionally, the database includes cross sectional area, A_i, and particle mass, m_i, at predefined humidity grids.

https://doi.org/10.5194/gmd-2022-153
Preprint. Discussion started: 1 July 2022

Geoscientific Model Development Discussions
Open Access
EGU

The extinction cross-section is calculated as

$$\sigma_{ei}(\lambda, h) = Q_{ei}(\lambda, h)\, A_i(h)\, m_i(0)\ , \tag{6}$$

where h is humidity, $m_i(0)$ is dry mass of tracer i, $i = 1, 2, \ldots, 15$. Here and thereafter, cross sectional area, A_i, is given per kg dry mass. Replacing $Q_{ei}(\lambda, h)$ in Eq. (6) with $Q_{si}(\lambda, h)$, the scattering cross-section, $\sigma_{si}(\lambda, h)$, for tracer i is obtained.

In order to calculate the extinction coefficient one needs to calculate tracer number density

$$N_i(z) = \frac{r_i(z)\, \rho_{air}(z)}{m_i(0)}\ , \tag{7}$$

where $r_i(z)$ is mass-mixing ratio, $\rho_{air}(z)$ is the air density, z is the altitude. The air density and mass-mixing ratio for all tracers are obtained from the MERRA input data file. The extinction coefficient of tracer i is given by

$$e_i(\lambda, z) \ = \ \sigma_{ei}(\lambda, h_z)\, N_i(z)\ , \tag{8}$$

and extinction coefficient of MERRA aerosol type is

$$e(\lambda, z) \ = \ \sum_{i=1}^{15} \sigma_{ei}(\lambda, h_z)\, N_i(z)\ , \tag{9}$$

where $\sigma_{ei}(\lambda, h_z)$ is obtained after interpolation of $\sigma_{ei}(\lambda, h)$ given by Eq. (6) on the humidity at altitude z which is given in the MERRA input data file. The scattering coefficient of tracer i, $s_i(\lambda, z)$, and total scattering coefficient, $s(\lambda, z)$, are calculated similar to Eqs. (8) and (9) replacing $\sigma_{ei}(\lambda, h_z)$ by $\sigma_{si}(\lambda, h_z)$. The phase function (scattering matrix element 11) for MERRA aerosol type is calculated as follows:

$$F(\lambda, z) \ = \ \frac{1}{s(\lambda, z)} \sum_{i=1}^{15} s_i(\lambda, z)\, F_i(\lambda, z)\ , \tag{10}$$

where $F_i(\lambda, z)$ is a scattering matrix element of tracer i.

In order to use MERRA aerosol type within SCIATRAN, the user needs to prepare Mass-Mixing Ratio (MMR) file for a given time and geographical location.

https://doi.org/10.5194/gmd-2022-153
Preprint. Discussion started: 1 July 2022

Geoscientific Model Development Discussions
Open Access
EGU

Table 5: Maximal and minimal radius of the particle size bins for dry sea salt and dust

Bin number	Dry sea salt		Dust	
	r_{min} (μm	r_{max} (μm)	r_{min} (μm)	r_{max} (μm)
1	0.03	0.1	0.1	1.0
2	0.1	0.5	1.0	1.8
3	0.5	1.5	1.8	3.0
4	1.5	2.0	3.0	6.0
5	5.0	10.0	6.0	10.0

To facilitate the usage of this aerosol type for inexperienced users, MMR files for typical aerosol scenarios (e.g. dust, biomass burning, urban pollution, and sea salt) are included in the SCIATRAN database. Details of how to prepare the MMR file as a SCIATRAN input for specific time and geographical location can be found in the user guide and in headers of MMR files for typical aerosol scenarios.

The MERRA aerosol type is operationally used to derive NASA MERRA aerosol properties dataset. The MERRA aerosol data products are widely used in the IPCC report (Randles et al., 2017).

Implementations of other aerosol types in SCIATRAN are on-going. For instance, the use of Aerosol Robotic Network (AERONET) measurement data (e.g. RI and PSD) as direct input for the radiative transfer simulations. The users are also encouraged to send their own ideas and requests to us.

4.2. Clouds and snow

The SCIATRAN software package includes water droplets and ice crystals optical parameters database (scattering matrices, scattering and extinction cross sections), which enables to calculate radiative transfer through liquid water, ice, mix-phase clouds and snow layers. Additionally, an absorber (e.g. soot) within cloud layer (Rozanov et al., 2014) can be accounted for.

https://doi.org/10.5194/gmd-2022-153
Preprint. Discussion started: 1 July 2022

4.2.1. Liquid water cloud database

The version of SCIATRAN described by (Rozanov et al., 2014) includes optical parameters (scattering matrices, extinction and scattering cross-sections) of water droplets with effective radius between 4 and 20 μm (in step of 2 μm) in the spectral range from 0.2 to 40 μm. The new implementation extends the database for the effective radius between 2 and 40 μm. The optical properties of liquid water cloud are pre-calculated using the Mie code (Mishchenko et al., 1999). The refractive index of pure water was selected according to Segelstein (1981). The water droplet size distribution was assumed to be gamma distribution:

$$f(r) \;=\; \frac{N_d\, r^{\eta}}{\Gamma(\eta+1)} \left(\frac{\eta}{r_m}\right)^{\eta+1} \exp\left(-r\frac{\eta}{r_m}\right) , \qquad (11)$$

where N_d is the number density of water droplets, r_m and η are the mode radius and half-width parameter, respectively, $\Gamma(\eta+1)$ is the gamma function. As in the previous version of SCIATRAN, the half-width parameter is set to 6. Recall that the relationship between mode radius and effective radius, r_e, is given by $r_e = r_m\,(1+3/\eta)$.

The SCIATRAN software offers the possibility to introduce a vertical inhomogeneity within a liquid water cloud considering N_d and r_e as functions of altitude. At the same time, the vertical coordinate, z, within a cloud is defined by employing the concept of dimensionless "altitude" as suggested by Feigelson (1981), i.e. it is introduced as $x = (h_t - z)/(h_t - h_b)$, where h_t and h_b are the top and bottom heights of the cloud layer, respectively. Thus, to introduce an inhomogeneity the user needs to specify $N_d(x)$ and $r_m(x)$ as functions of the dimensionless coordinate x, which ranges from 0 to 1.

The water droplet database within SCIATRAN software was employed e.g. to derive the cloud optical thickness, liquid water cloud droplets effective radius in the framework of the XBAER algorithm (Mei et al., 2019) and vertical profile of droplets effective radius (Kokhanovsky and Rozanov, 2012).

https://doi.org/10.5194/gmd-2022-153
Preprint. Discussion started: 1 July 2022

4.2.2. Ice cloud and snow layer database

The previous ice cloud database in SCIATRAN only included optical parameters of two ice crystal shapes, namely fractal of second generation (Macke et al., 1996) and hexagonal prisms. Moreover, the optical characteristics were pre-calculated within a limited range of ice crystal size. In particular, for second generation fractal the tetrahedron side length was set to 50, 100 and 300 μm, which corresponds to the effective radius of 23, 46 and 142 μm, respectively. For hexagonal prisms, the optical properties were pre-calculated for hexagonal prism height of 100 μm and side lengths of 12.5, 25 and 50 μm.

The limited range of ice crystal sizes can introduce large uncertainties in the ice cloud effective radius retrieval (Mei et al., 2018a). To overcome this problem, ice crystal databases developed by Baum et al. (2011) and Yang et al. (2013) were also included in the SCIATRAN software. These ice cloud databases were operationally used to derive NASA cloud properties dataset from MODIS (King et al., 2013, Platnick et al., 2017).

The Baum ice crystal database contains optical parameters of "AggregateSolidColumns" shape of ice crystals in the spectral range 0.2 - 99 μm with effective radius between 5 and 60 μm, and the step of 2.5 μm.

The Yang database consists of optical parameters of nine ice crystal shapes, i.e. aggregate of 8 columns, droxtal, hollow bullet rosettes, hollow column, plate, aggregate of 5 plates, aggregate of 10 plates, solid bullet rosettes, and column. The optical parameters include extinction efficiency, extinction cross-section, single scattering albedo and six elements of the scattering matrix pre-calculated for maximal dimension of ice habits between 2 and 10000 μm in the spectral range from 0.2 to 15.25 μm. Details of Yang database implementation into the SCIATRAN software can be found in Pohl et al. (2020).

It is worth noticing that for the same maximal dimension of ice crystal, its effective radius depends on its shape. For instance, the maximal dimension of 700 μm results in effective radius of 295.3 μm for droxtal whereas it is 53.0 μm for plate. The relationship between maximal dimension and effective radius for

https://doi.org/10.5194/gmd-2022-153
Preprint. Discussion started: 1 July 2022

Geoscientific Model Development Discussions

crystals of different shape can be found in Yang et al. (2013) and also included in the SCIATRAN database.

Natural ice cloud layers are usually composed of polydisperse ice crystals of different shapes (Baum et al., 2005). For Yang database, the polydispersity and habit mixture, can be considered in SCIATRAN using PSD function and a desired habit ratio, respectively. In particular, to describe polydisperse properties of habit mixture, the gamma distribution with respect to the maximal dimension, D, following Saito et al. (2019), is used:

$$n(D) = N_c\, C\, (D/D_0)^{k-1}\, \mathrm{e}^{-(k-1)\, D/D_0}\ . \tag{12}$$

Here, N_c is the number of ice crystals per unit volume, k and D_0 are the shape and mode parameters, C is the normalization factor. The number density, N_c, and mode, D_0, can be selected as constant within ice cloud layer or depending on the altitude. This enables to formulate a realistic model of a vertically inhomogeneous, polydisperse crystal habit mixture of an ice cloud and snow layer.

Similar to the snow grain habit mixture model used by Saito et al. (2019), the habit mixture implemented into SCIATRAN depends on the dimension of ice crystals. In particular, user can pre-define mixing ratios $f_h(D_i)$ of any aforementioned ice particle habit, h, at specific dimension grid point D_i, defined in Yang database. SCIATRAN interpolates the mixing ratios linearly with respect to $\ln D$ between division points and calculates the bulk optical properties of ice particle habit mixture by weighting the single-habit properties according to their mixing ratio. Following Baum et al. (2011), the scattering and extinction cross-sections as well as the scattering matrix are calculated as:

$$\sigma_p = \sum_{h=1}^{N_h} \int_{D_1}^{D_2} f_h(D)\, \sigma_{p,h}(D)\, n(D)\, dD\ , \tag{13}$$

$$\mathbf{F}(\gamma) = \frac{1}{\sigma_s} \sum_{h=1}^{N_h} \int_{D_1}^{D_2} f_h(D)\, \mathbf{F}_h(\gamma, D) \sigma_{s,h}(D)\, n(D)\, dD\ , \tag{14}$$

https://doi.org/10.5194/gmd-2022-153
Preprint. Discussion started: 1 July 2022


Geoscientific Model Development Discussions
Open Access
EGU

where N_h is the number of habits, the subscript p denotes 's' or 'e' for the scattering, $\sigma_{s,h}(D)$, or extinction, $\sigma_{e,h}(D)$, cross-section, respectively, $\mathbf{F}_h(\gamma, D)$ is the scattering matrix of habit h having dimension D, and

$$\sum_{h=1}^{N_h} f_h(D) \;=\; 1\,. \tag{15}$$

The integrals in Eqs. (13) and (14) are calculated by SCIATRAN numerically using trapezoidal rule and partition of the interval $[D_1 = 2\,\mu m, D_2 = 10000\,\mu m]$ is performed according to the discrete grid used by Yang et al. (2013). In particular, the intervals are 1, 2.5, 12.5, 125 μm for ranges [2 - 10], [10 - 100], [100 - 1000], [1000 - 10000] μm, respectively.

As mentioned above, the SCIATRAN software enables the user to introduce a vertical inhomogeneity within an ice cloud or snow layer considering N_c and D_0 as functions of depth. In this case the approach of dimensionless "altitude" is employed as described above for a liquid water cloud. Thus, the user needs to specify $N_c(z)$ and $D_0(z)$ as functions of the dimensionless coordinate x, which ranges from 0 to 1.

For a vertically homogeneous mono-disperse habit-mixture cloud, the input parameters include the optical thickness of the cloud, maximal dimension and fraction of selected ice crystal shapes. Combing the liquid water and ice crystals optical properties, the radiative transfer calculations can also be performed through a mix-phase cloud.

The database of the optical properties of ice crystals proposed by Yang et al. (2013) was successfully utilized to 1) estimate impact of habit mixture on the simulation of Top Of the Atmosphere (TOA) reflectance from Polarization and directionality of Earth reflectances (POLDER) measurements (Pohl et al., 2020); 2) derive snow properties research products (snow grain size and shape) using the TOA reflectance measurements provided by Copernicus Sentinel-3 Sea and Land Surface Temperature radiometer (SLSTR) instrument in the framework of the XBAER algorithm (Mei et al., 2021a,b).

Although it has been demonstrated that the database of the optical properties of ice crystals proposed by Yang et al. (2013) can be used for snow studies, a

https://doi.org/10.5194/gmd-2022-153
Preprint. Discussion started: 1 July 2022


Geoscientific Model Development Discussions

realistic model of a snow layer is usually represented by a vertically inhomogeneous, polydisperse ice crystal habit mixture (Mei et al., 2021a), which requires a-priori knowledge of several properties of the snow layer (e.g., appropriate numbers of habits and their fraction as well as parameters of PSD function). To simplify the requirements for such a-priori knowledge, we have also implemented a stochastic mixture model of ice crystals and air gaps in SCIATRAN. In this case the snow layer is considered as a porous material and the model of a random mixture based on the stereological approach is applied (Malinka, 2014). With an assumption of stochastic ice crystal mixture, this approach uses the concept of the chord length distribution rather than the characteristics of a separate crystal. The theoretical background to calculate optical parameters of corresponding stochastic snow model can be found in Malinka (2014, 2015). The usage of stochastic model has at least two advantages as compared to Yang et al. (2013) database. First, the stochastic model does not require any database because the optical parameters can be easily calculated online. Second, for a vertically homogeneous snow layer, users only need to have information about mean chord of ice crystals and the optical thickness of the snow. The mean chord length plays the role of the effective size of a grain, namely mean chord coincides with the factor of 3/4 with the standard definition of the effective radius (Malinka, 2014).

4.3. Surface reflection

Surface albedo or BRDF are important parameters in RT calculations. The SCIATRAN software includes both Lambertian albedo and various BRDF models (Rozanov et al., 2014). In the case of Lambertian reflection, user can select spectral dependent or constant albedo. In particular, global dataset of vegetation and land albedo (Matthews, 1983) is available in the SCIATRAN software. For RT calculations accounting for a surface BRDF, users can choose one of the following build-in models: RPV, modified RPV, Kernel-based Ross-Li

https://doi.org/10.5194/gmd-2022-153
Preprint. Discussion started: 1 July 2022


Geoscientific Model Development Discussions

vegetation-soil, modified RPV plus facet (Rahman et al., 1993, Maignan et al., 2004, Roujean et al., 1992, Breon and Vermote, 2012, Vermote et al., 2009). For a retrieval of surface properties from satellite observations, the following surface reflectance models are additionally included in SCIATRAN: PROSAIL, XBAER, snow and melt ponds on sea ice.

4.3.1. PROSAIL model for vegetated surfaces

The PROSAIL model is a combination of the PROSPECT and SAIL (Scattering by Arbitrary Inclined Leaves) models (Jacquemound et al., 2009). The PROSAIL is used to describe the directional reflectance of plant canopy and retrieve biophysical properties of vegetation.

The PRO4SAIL source code (http://osr-cesbio-ups-tlse.fr) was adopted and implemented into the SCIATRAN software. The input parameters are leaf inclination distribution function type, Leaf Area Index (LAI), hot spot parameter, chlorophyll content, carotenoid content, brown pigment content, Equivalent Water Thickness (EWT), Leaf Mass per Area (LMA), structure coefficient and soil factor.

Using a desired model of the atmosphere in combination with BRDF provided by the implemented PROSAIL model, user can calculate the radiation field in the atmosphere in UV, VIS, and NIR spectral ranges accounting for the angular scattering properties of a vegetated surface. To verify the implementation of the PROSAIL model, a comparison of TOA reflectances simulated by SCIATRAN and measured by the MODIS instrument is presented in Sect. 6 (see upper panel of Fig. 5).

4.3.2. XBAER land surface reflectance parameterization

The XBAER model describes the surface reflectance by a linear relationship with respect to Soil Adjusted Vegetation Index (SAVI) (Mei et al., 2017a).

https://doi.org/10.5194/gmd-2022-153
Preprint. Discussion started: 1 July 2022


Geoscientific Model Development Discussions

This model was originally designed for the AOT retrieval in the framework of the XBAER algorithm(Mei et al., 2017a) using measurements of the MERIS instrument. For wavelengths above the red-edge (MERIS channels 10, 12, 13 and 14, which correspond to 753, 778, 865 and 885 nm), the surface reflectance, $R(\lambda_i)$, was approximated as

$$R(\lambda_i) \;=\; a(\lambda_i)\,x + b(\lambda_i), \quad i = 10, 12, 13, 14, \tag{16}$$

where i is the MERIS channel number, $a(\lambda_i)$ and $b(\lambda_i)$ are the slope and intercept for given wavelengths λ_i in the Surface Reflectance Wavelength Shape Constrain Database (SRWSCD) (Mei et al., 2017a) and x is SAVI.

For wavelengths below the red-edge (MERIS channels 1,2,...,9, which correspond to 412, 443, 490, 510, 560, 620, 665, 681 and 708 nm), the ratio between the surface reflectance at each wavelength, λ_i, and the surface reflectance at the MERIS channel 14 was parameterized by

$$R(\lambda_i)/R(\lambda_{14}) \;=\; \tilde{a}(\lambda_i)\,x \;+\; \tilde{b}(\lambda_i), \quad i = 1, 2, ..., 9. \tag{17}$$

The SRWSCD database, which belongs to the XBAER retrieval algorithm and is not included in the SCIATRAN database, includes the geographic dependent monthly slope and intercept of the linear model.

Regression coefficients for typical surface types (e.g. vegetated surface, urban, desert) are included in the SCIATRAN database. Using the data files for these typical surface types as templates, users can prepare their own regression coefficients following Mei et al. (2017a).

A comparison of simulated TOA reflectances obtained utilizing XBAER parameterization and PROSAIL model are presented in Sect. 6 (see upper panel of Fig. 5).

4.3.3. Snow and melt ponds on sea ice

Besides the modified RPV (Degunther and Meerkotter, 2000) and asymptotic model (Kokhanovsky and Zege, 2004) of the snow reflectance, the recent snow

https://doi.org/10.5194/gmd-2022-153
Preprint. Discussion started: 1 July 2022


Geoscientific Model Development Discussions

kernel-based BRDF models, such as RTLSRS and FASMAR suggested by Jiao et al. (2019) and Mei et al. (2022), respectively, as well as the model of white ice and melt ponds on sea ice (Malinka et al., 2016, 2018) were also included.

RTLSRS model.

The kernel-driven RossThick-LiSparseReciprocal BRDF model with snow kernel (RTLSRS) (Jiao et al., 2019) was implemented in the following form:

$$\rho(\Omega,\lambda) \;=\; f_i(\lambda) + f_v(\lambda)K_v(\Omega) + f_g(\lambda)K_g(\Omega) + f_s(\lambda)K_s(\Omega)\;, \qquad (18)$$

where f_i, f_v, f_g, and f_s are wavelength-dependent coefficients, Ω comprises angular variables $\{\vartheta_0, \vartheta, \varphi\}$, which describe solar zenith angle, viewing zenith angle and relative azimuth, respectively, λ is wavelength, K_v, K_g, and K_s are the volumetric scattering kernel, geometric-optical kernel and snow kernel, respectively.

As compared to the classical Ross-Li model suggested by Lucht et al. (2000), an additional snow kernel based on the asymptotic model of Kokhanovsky and Zege (2004) was introduced to describe the strong forward scattering peak typical for the snow reflection. Although the SCIATRAN software does not contain a database of the coefficients $f_i(\lambda)$, $f_v(\lambda)$, $f_g(\lambda)$, and $f_s(\lambda)$, the kernels are included. The user needs to provide a file containing the coefficients at a discrete number of wavelengths. Some examples of the coefficients obtained by fitting the RTLSRS model to the measured TOA reflectance are presented in Jiao et al. (2019). The file structure is described in the user guide.

FASMAR.

In contrast to the RTLSRS model, where the show kernel based on the ART model (Kokhanovsky and Zege, 2004) was used to improve the accuracy in the case of a snow reflection, FASMAR exploits the ART model as a main kernel. In particular, FASMAR (see Mei et al. (2022) for details) includes 4 kernels and the model is formulated as

$$\rho(\Omega,\lambda) \;=\; f_1 + f_2\,K_2(\Omega,\lambda) + f_3\,K_3(\Omega,\lambda) + f_4\,K_4(\Omega) + f_5\,K_5(\Omega)\;, \qquad (19)$$

https://doi.org/10.5194/gmd-2022-153
Preprint. Discussion started: 1 July 2022

Geoscientific Model Development Discussions
Open Access
EGU

where $f_1, f_2, \ldots, f_5$ are wavelength dependent parameters (argument λ is omitted), and the kernels are given by

$$K_2(\Omega,\lambda) = R^0_\infty(\Omega)\,\mathrm{e}^{-\beta_\lambda\,A(\Omega)} - k_2(\lambda)\,, \tag{20}$$

$$K_3(\Omega,\lambda) = p_\lambda(\theta)/(\mu+\mu_0)/4 - k_3(\lambda)\,, \tag{21}$$

$$K_4(\Omega) = R^0_\infty(\Omega)\,\mathrm{e}^{\cos\theta} - k_4\,, \tag{22}$$

$$K_5(\Omega) = \cos\theta - k_5\,. \tag{23}$$

In the right hand side of each equation the second term is introduced which modifies the respective kernel to obtain $K_2 = K_3 = K_4 = K_5 = 0$ for SZA=0° and VZA=0°. The modification terms are given by

$$k_2(\lambda) = R^0_\infty(\tilde{\Omega})\,\mathrm{e}^{-\beta_\lambda\,A(\tilde{\Omega})}\,,\; k_3(\lambda) = \frac{p_\lambda(-1)}{8}\,,\; k_4 = \frac{R^0_\infty(\tilde{\Omega})}{2.718}\,,\; k_5 = -1\,. \tag{24}$$

As a result, the coefficient f_1 gives the magnitude of the reflectance in the nadir direction (Roujean et al., 1992). In Eqs. (20)-(24), $\mu = \cos\vartheta$, $\mu_0 = \cos\vartheta_0$, ϑ_0, ϑ and θ are solar zenith angle, viewing zenith angle and scattering angle, respectively, $\tilde{\Omega} = \{0,0,0\}$, $\beta_\lambda = \sqrt{\gamma_\lambda\,d}$, $\gamma_\lambda = 4\pi\,\kappa_i/\lambda$ is the absorption coefficient of ice, κ_i is the imaginary part of the ice refractive index, d is an effective grain size, defined by the ratio of the average volume to the average surface area of grains, $p_\lambda(\theta)$ is the phase function, and $R^0_\infty(\Omega)$ is the reflection function of semi-infinite non-absorbing media.

FASMAR includes the ART kernel, K_2, a single-scattering kernel, K_3, and auxiliary kernels, K_4 and K_5. The kernel K_5 is only used for wavelengths longer than 1600 nm. In kernel K_2, the function $R^0_\infty(\Omega)$ is implemented according to the approximation suggested by Kokhanovsky (2005), the function $A(\Omega)$ is given by $A(\Omega) = b_n\,K_0(\mu)\,K_0(\mu_0)/R^0_\infty(\Omega)$ (Kokhanovsky and Zege, 2004), where $K_0(\mu)$ is called the escape function, which is implemented according to the common approximation (Sobolev, 1972) as $K_0(\mu) = 3/7(1+2\mu)$. The parameter b_n depends mainly on the ice crystal shape. For the fractal ice particles, it was estimated by Kokhanovsky and Zege (2004) to be 3.62. As a result, the final expression for $A(\Omega)$ is given by $A(\Omega) = 0.66\,(1+2\mu)(1+2\mu_0)/R^0_\infty(\Omega)$.

https://doi.org/10.5194/gmd-2022-153
Preprint. Discussion started: 1 July 2022


Geoscientific Model Development Discussions
Open Access
EGU

Similar to the RTLSRS model, the SCIATRAN software does not contain database of the coefficients $f_1, f_2, \ldots, f_5$. The user needs to provide a file containing the coefficients at a discrete number of wavelengths. The file structure is described in the user guide.

Comprehensive comparisons of FASMAR and RTLSRS models with ground-based, aircraft and satellite measurements of snow angular reflectance can be found in Mei et al. (2022). FASMAR can be used for large solar zenith angles (e.g. SZA $> 80°$, which is a typical case the polar regions) while both Ross-Li and the RTLSRS models are recommended to be used for SZAs $< 70°$.

White ice and snow-covered ice reflectance model.

White ice and snow-covered ice are two typical surface types in the polar regions. Following Malinka et al. (2016), the white ice model describes an ice layer with a highly scattering granular layer on top. Since the grain size of ice crystals is significantly larger than the wavelength of incident light, the optical parameters (extinction coefficient, SSA, and phase function) of a stochastic mixture of irregular ice crystals and air gaps can be analytically derived following Malinka (2014, 2015). Using the analytical expressions for optical parameters and employing asymptotic radiative transfer theory, the following analytical expression for BRDF of white ice was proposed by Malinka et al. (2016) and implemented into SCIATRAN:

$$R = R^0_\infty \, \frac{\sinh\left(\gamma\,\tau + y\,[1 - K(\vartheta)K(\vartheta_0)/R^0_\infty]\right)}{\sinh(\gamma\,\tau + y)}\,, \tag{25}$$

where R^0_∞ is the BRDF of a non-absorbing semi-infinite layer with the same scattering phase function as the snow layer, sinh denotes the sinus hyperbolicus, τ is optical thickness of the snow layer, ϑ_0 and ϑ are incidence and observation polar angles, respectively,

$$\gamma = \sqrt{3\,(1-\omega)\,(1-\omega\,g)}\,, \qquad K(\vartheta) = \frac{3}{7}\,(1 + 2\,\cos\vartheta)\,, \tag{26}$$

$$y = 4\,\sqrt{\frac{(1-\omega)}{3\,(1-\omega\,g)}}\,, \qquad K(\vartheta_0) = \frac{3}{7}\,(1 + 2\,\cos\vartheta_0)\,. \tag{27}$$

https://doi.org/10.5194/gmd-2022-153
Preprint. Discussion started: 1 July 2022

Geoscientific Model Development Discussions

The expression for the single scattering albedo is

$$\omega = 1 - \frac{\alpha\, n^2\, a\, T_{dif}}{\alpha\, n^2\, a + T_{dif}}\ , \qquad \alpha = \frac{4\,\pi\,\kappa}{\lambda} + \alpha_y\ , \tag{28}$$

where n and κ are the real and imaginary parts of the ice refractive index, a is mean chord of ice crystals and α_y is the absorption by the yellow substance in the white ice. Analytical expressions for g, α_y, and auxiliary function T_{dif} are given in Sect. 8.1.

The usage of Eq. (25) to calculate BRDF in the framework of SCIATRAN software requires the following parameters to be provided by the user: optical thickness of the snow layer, τ, mean chord of ice crystals, a, and yellow substance absorption coefficient, α_y. The refractive index of ice can be either taken from the SCIATRAN database or provided by the user. The calculation of R^0_∞ is performed by SCIATRAN using a pre-calculated look-up-table.

Melt ponds on sea ice reflectance model.

The BRDF model of melt ponds on sea ice as derived by Malinka et al. (2018) was implemented into SCIATRAN as follows:

$$R_\lambda(\Omega) = \frac{1}{\mu_0}\, R_F(\mu_0)\, \delta(\mu - \mu_0)\, \delta(\varphi) + \frac{T_F(\mu)\, T_F(\mu_0)\, A_b}{\pi n^2 [1 - A_b\, f_{in}(\tau_p)]}\, e^{-\tau_p/\mu'_0 - \tau_p/\mu'}\ . \tag{29}$$

Here, $R_F(\mu_0)$ and $T_F(\mu_0)$ are the Fresnel reflectance and transmittance of a flat water surface for the cosine of the incidence angle μ_0, n is the refractive index of water (assuming refractive index of air to be 1), μ'_0 is the cosine of the refractive angle ($\sqrt{1-\mu_0^2} = n\sqrt{1-\mu_0'^2}$) , $\tau_p = z\,\sigma_p$ is the optical thickness of pond, z is the pond depth and σ_p is the extinction coefficient of the water, equal to the sum of the water absorption (α_w) and scattering (σ_w) coefficients, A_b is the pond bottom albedo. The auxiliary function $f_{in}(\tau_p)$, as given in Malinka et al. (2018), is calculated numerically by the SCIATRAN program. For simplicity reasons, the dependence of R_F, T_F, A_b, n, and τ_p on the wavelength, λ, is not indicated. The analytical expression for albedo of an under-pond ice layer A_b as a function of the geometric thickness of under-pond ice, H, and transport scattering coefficient, σ_t is given in Appendix.

To calculate BRDF using Eq. (29) in the framework of the SCIATRAN software

https://doi.org/10.5194/gmd-2022-153
Preprint. Discussion started: 1 July 2022


Geoscientific Model Development Discussions
Open Access
EGU

the following input parameters need to be provided by the user: geometric thickness of the under-pond ice, H, water layer (pond) depth, z, and transport scattering coefficient, σ_t. Following Malinka et al. (2018), the reasonable range for σ_t is [0.2 - 10] m^{-1}. In particular, for light and dark melt ponds, typical values for σ_t are ~ 4 and $\sim 2\,\mathrm{m}^{-1}$, respectively. Water absorption and scattering coefficients as well as refractive indices of water and ice can be either taken from SCIATRAN databases or provided by the user.

5. Inherent optical properties of aerosol and clouds

5.1. Aerosol

Fig. 3 shows an example of the optical properties of the newly implemented in SCIATRAN aerosol types. All optical properties are calculated using AOT of 0.5 at the wavelength of 0.55 μm. For MODIS-DT, moderately absorbing aerosol type is selected. For MODIS-OC, two basic components F1 and C2, see Table 3, are selected and the fine mode fraction is set to 0.5. For XBAER-OC, purely maritime aerosol type is selected. For Dubovik dust model, the aspect ratio is set to 1. For OPAC 4.0 dust model, the total number of mineral particles is set to 300 representing the "background desert conditions" (Köpke et al., 2015). The MERRA aerosol type is selected for the AERONET site Rio-Branco (-67.869°E, -9.957°N) on 16 August, 2020. With the above settings, the MODIS-DT and MERRA (picked up at the same time and location), MODIS-OC and XBAER-OC (both represent the maritime aerosol type), Dubovik dust and OPAC 4.0 dust (both represent the dust aerosol type) are pairs whose optical properties are expected to be comparable.

In Fig. 3(a), the wavelength dependent AOTs calculated using different aerosol types show the same value at 550 nm because all optical properties are scaled to AOT = 0.5 at this wavelength. The Angstrom coefficients (in the spectral range 440 - 870 nm) are 1.77 and 1.81 for MODIS-DT and MERRA, -0.19 and -0.11

https://doi.org/10.5194/gmd-2022-153
Preprint. Discussion started: 1 July 2022


Geoscientific Model Development Discussions
Open Access
EGU

for MODIS-OC and XBAER-OC, 0.56 and 0.01 for Dubovik dust and OPAC 4.0 dust, respectively. The lines of the MODIS-DT and MERRA aerosol types almost overlap, indicating the similarity of aerosol properties between MODIS-DT and MERRA. MODIS-OC and XBAER-OC show a similar spectral pattern with AOT slightly increasing with the wavelength. This can be explained by the significant contribution of coarse mode particles. The Dubovik dust shows a much stronger spectral gradient as compared to OPAC 4.0 dust.

Fig. 3(b) shows the phase functions at 550 nm for the selected aerosol types. In the case of MERRA, the phase function is selected for an altitude near the surface. As expected, MODIS-DT and MERRA, MODIS-OC and XBAER-OC, Dubovik and OPAC 4.0 dust have similar phase functions, respectively. Coarse-mode dominated aerosol types (MODIS-OC, XBAER-OC, Dubovik and OPAC 4.0) show stronger forward peak scattering as compared to fine-mode dominated aerosol types (MODIS-DT and MERRA). For the selected scenario, MODIS-DT shows a stronger forward scattering and a weaker backward scattering as compared to MERRA. MODIS-OC and XBAER-OC, with completely different paramterization strategies, show very similar phase functions. Dubovik and OPAC 4.0 dust models show relatively large difference in the forward scattering as compared to other aerosol types (e.g. MODIS-DT and MERRA, XBAER-OC and MODIS-OC).

Fig. 3(c) shows the wavelength-dependent Single Scattering Albedo (SSA) for the selected aerosol types. MODIS-DT and MERRA show large difference in the absolute SSA values, however, both demonstrate the increase of absorption with the wavelength. MODIS-OC and XBAER-OC, especially XBAER-OC, demonstrate weak absorption. The Dubovik and OPAC 4.0 dust models show again differences in both magnitude and wavelength dependence.

Fig. 3(d) shows the wavelength dependent asymmetry factor, g, for the selected aerosol types, which is a fundamental property of aerosol particle that affects the aerosol direct radiative forcing. MODIS-OC and XBAER-OC show the largest g values indicating a stronger forward scattering while MODIS-DT and MERRA show the smallest g indicating a weaker forward scattering, which is

https://doi.org/10.5194/gmd-2022-153
Preprint. Discussion started: 1 July 2022

Geoscientific Model Development Discussions

consistent with the results presented in Fig. 3(b).

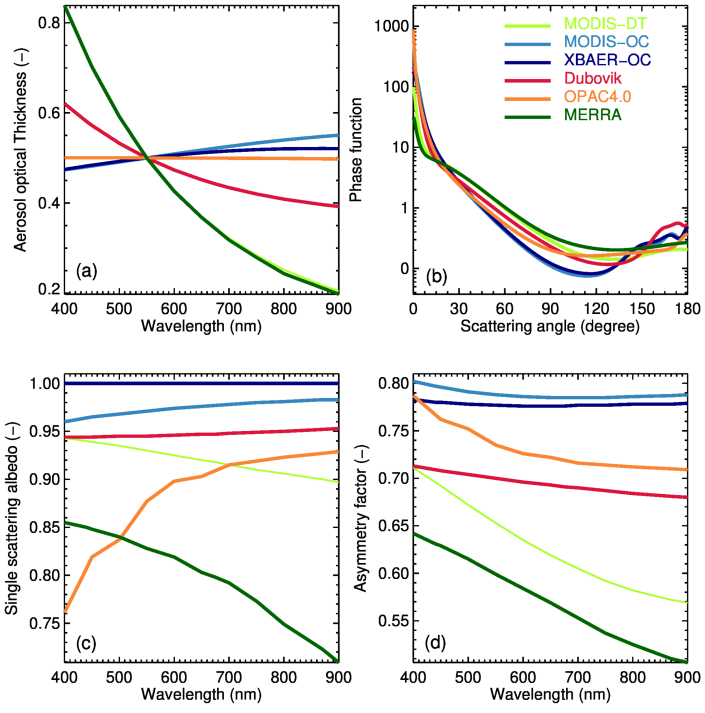

Figure 3: Optical properties of the newly implemented in SCIATRAN aerosol types (indicated by different colors): (a) wavelength dependent AOT; (b) phase function at a wavelength of 0.55 μm; (c) wavelength dependent single scattering albedo; (d) wavelength dependent asymmetry factor

5.2. Cloud

A comprehensive consideration of the extinction efficiency, single-scattering albedo, and asymmetry factor for different wavelengths, maximum dimensions, and selected crystal shapes can be found in Yang et al. (2013). In the scope

https://doi.org/10.5194/gmd-2022-153
Preprint. Discussion started: 1 July 2022


Geoscientific Model Development Discussions
Open Access
EGU

of this paper we consider only the phase functions of ice crystals in the visible spectral range, where, owing to weak absorption by ice and water, the scattering processes plays very important role.

Fig. 4 shows the comparison of water droplets and ice crystals phase functions with campaign measurements provided by Jarvinen et al. (2018). The phase functions are presented at the wavelength of 532 nm and normalized to the Arctic CLoud Observations Using airborne measurements during polar Day (ACLOUD) measurement at scattering angle of 18 ° (Jarvinen et al., 2018). The effective radii of water droplets and ice crystals are selected to be the global mean values of about 13.5 μm and 25 μm, respectively (King et al., 2013).

As expected, the phase function of water droplets is quite different from those of ice crystals, especially at backward scattering directions. In particular, the famous rainbow feature of the scattering by water droplets can be observed at about 138°. The large differences in the phase functions observed by different campaigns indicates the large variability of cloud optics. Large differences are observed mainly in the backward scattering direction. For ice crystals, aggregate of 8 columns and droxtal have the strongest backward scattering while plate shows the weakest one. The large variability of the campaign measurements can be well described by a mixture of different ice crystal shapes.

6. Simulated TOA reflectance for different CAS scenarios

In this section we consider selected applications of aerosol and cloud databases and BRDF models for calculations of TOA reflectance for a surface-atmosphere system using SCIATRAN software. The following surface scenarios are considered below: snow, white ice and melt ponds typical for high latitude regions and vegetated surface typical for low and middle latitude regions.

Vegetated surface

Simulations presented in this sub-section are performed using the veiwing geom-

https://doi.org/10.5194/gmd-2022-153
Preprint. Discussion started: 1 July 2022

Geoscientific Model Development Discussions
Open Access
EGU

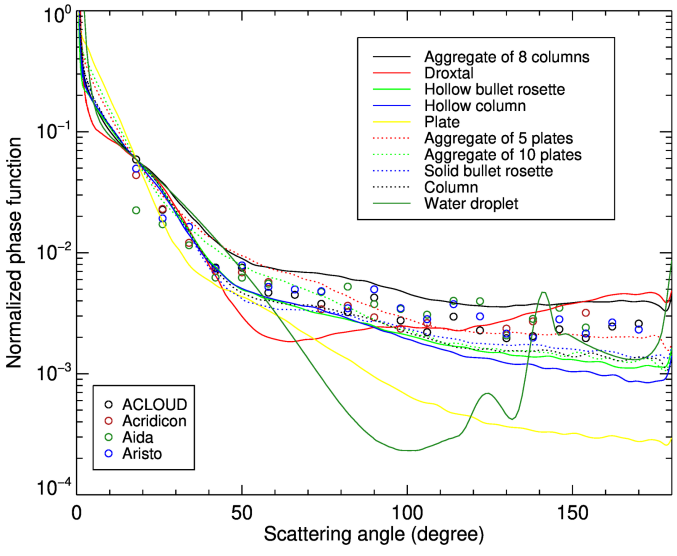

Figure 4: Comparison of phase functions for water droplets and ice crystals with campaign measurements provided by Jarvinen et al. (2018). Symbols - measurements, lines - different shapes.

https://doi.org/10.5194/gmd-2022-153
Preprint. Discussion started: 1 July 2022


Geoscientific Model Development Discussions
Open Access
EGU

etry and the spectral responce function of the HyperSpectral Imager (HSI) instrment onboard the Environmental Mapping and Analysis Program (EnMAP) mission. HSI/EnMAP is a German perspective mission to monitor environment-related parameters launched in April 2022 and XBAER is a candidate algorithm to provide CAS products for this instrument (a proposal is under review to the time of writing).

Example simulations of the TOA reflectance with SCIATRAN for different scenarios were performed for the AERONET site Rio-Branco (-67.869°, -9.957°) in the Amazon region for 16 August, 2020. The surface reflectance was calculated by using either the XBAER paramterization or the PROSAIL model. The SAVI parameter required by the XBAER parameterization was estimated from measurements of the Ocean and Land Colour Instrument (OLCI) as 0.34. Due to database limitations the simulations using XBAER parameterization were done only for OLCI wavelengths. The PROSAIL model was used with LAI of 4.6, which was obtained from the MODIS LAI product. Leaf inclination distribution function type was set to Type = 1 (Spherical). Other parameters are set as follows: hot spot parameter (0.01); chlorophyll content ($1\,\mu g/cm^2$); carotenoid content ($8\,\mu g/cm^2$); brown pigment content (0); EWT (0.01 cm); LMA ($0.009\,g/cm^2$); structure coefficient (1.5); soil factor (1.0).

The aerosol was accounted for by using the MERRA aerosol type with fraction of each component provided by MERRA data base for the selected time and location. In particular, AOTs of the total column, Black Carbon, Organic Carbon, Sulfate, Sea Salt, and Dust are 0.241, 0.043, 0.143, 0.043, 0.003, and 0.009, respectively. A water cloud between 2.0 and 2.5 km with Cloud Optical Thickness (COT) of 3 and effective radius of water droplets of $13.5\,\mu m$ was used for simulations. Along with aerosol, cloud, and Rayleigh scattering the absorption by all relevant atmospheric gases was accounted for. The vertical profiles of pressure, temperature, and absorber number density were taked from the database calculated with Bremen 2D Chemical Transport Model (Sinnhuber et al., 2009) for August at the latitude of 10°S.

https://doi.org/10.5194/gmd-2022-153
Preprint. Discussion started: 1 July 2022


Geoscientific Model Development Discussions
Open Access
EGU

TOA reflectances simulated with SCIATRAN for different scenarios are shown in the upper panel of Fig. 5. For comparison, TOA reflectances measured by the MODIS instrument at the same time and location are also presented. One can see that for clear sky scenarios (S+R+A and S+R+A+G) the TOA reflectances simulated using both XBAER surface paramterization and PROSAIL model agree well with reflectances observed by MODIS. The red-edge effect and sharp spectral structures are from vegetation and gas absorption, respectively. The plot indicates that employing the newly implemented features in the SCIATRAN model, the wavelength dependence and the magnitude of TOA reflectance observed by MODIS can be well reproduced by the simulations.

For the cloudy scenario (S+R+A+G+C) one observes a general enhancement of the TOA reflectance caused by the additional reflectance of the cloud layer. However, the contribution of surface is still visible (red edge from vegetation) because the cloud is optically thin (COT = 3).

The MERRA aerosol model used for the simulations enables us to investigate contributions of different aerosol components to the TOA reflectance. For this purpose the TOA reflectance was calculated first accounting for the contributions from all aerosol components (total) and then for each particular aerosol component independently. The contributions of different aerosol components are illustrated in the lower panel of Fig. 5. The plot shows differences in the TOA reflectances calculated for single aerosol components with respect to the reflectance calculated accounting for all components. In the case under consideration (over the Amazon forest), the contribution of aerosol components differs for different wavelengths with the strongest contribution from organic carbon component below about 800 nm (smallest difference to the simulation with all components) and strongenst contribution from the black carbon component in 1000-1400 nm range.

Snow surface

This sub-section presents example results of simulations of snow reflectance performed with the radiative transfer package SCIATRAN. The snow layer was defined as a layer with an a optical thickness of 5000 and a geometrical

https://doi.org/10.5194/gmd-2022-153
Preprint. Discussion started: 1 July 2022

Geoscientific Model Development Discussions
Open Access
EGU

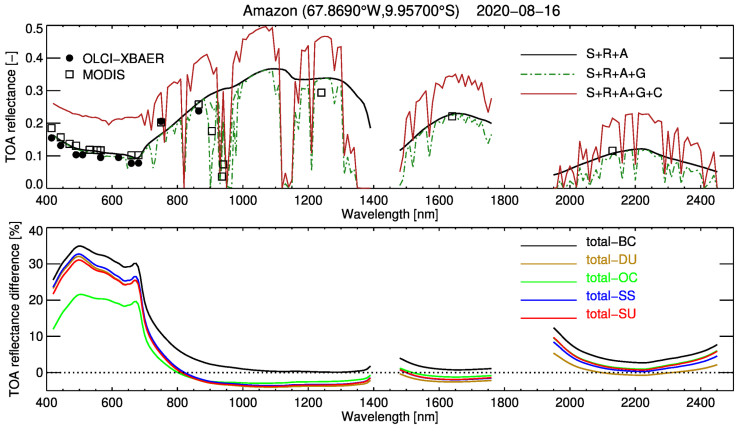

Figure 5: TOA reflectance simulation for a measurement from the EnMAP instrument over the Amazon region on 16 August, 2020. Upper panel: TOA reflectance simulated using different settings: S - surface reflectance described by the PROSAIL model, R - Rayleigh, A - Aerosol, G - Gaseous absorbers, C - Cloud. Open rectangles depict MODIS observation data and filled circles represent simulations with XBAER for OLCI wavelengths. Lower panel: contributions of different MERRA aerosol components to the simulated TOA reflectance: BC - Black Carbon, DU - Dust, OC - Organic Carbon, SS - Sea Salt, SU - Sulfate.

https://doi.org/10.5194/gmd-2022-153
Preprint. Discussion started: 1 July 2022


Geoscientific Model Development Discussions

thickness of 1 m covering a black surface. The snow layer was assumed to be vertically and horizontally homogeneous without any surface roughness and composed of monodisperse ice crystals. The impact of snow impurities and scattering/absorption processes in the atmosphere was neglected. Droxtal ice crystal shape with effective radius of 126 μm (Mei et al., 2021b) from the crystals optical properties database by Yang et al. (2013) was used for simulations. The solar zenith angle was set to 68.9°, which corresponds to the mean value during summer at Svalbard (Mei et al., 2022).

The BRDF of the show layer calculated with SCIATRAN is shown in the form of polar plots in the right column of Fig. 6 for wavelengths of 380, 480, 670, 870, 1220, and 2200 nm. These wavelengths are selected to represent typical spectral chanels of satellite instruments from UV to SWIR. For a comparison, the snow BRDF was calculated using FASMAR and RTLSRS models. The coefficients required by these models were obtained by fitting their results to SCIATRAN simulations. The results from FASMAR and RTLSRS models are presented in the middle and left columns of Fig. 6. One can see that reflectances obtained with FASMAR and RTLSRS models show very good agreement (both spectral and angular) with the SCIATRAN simulations. However, the RTLSRS model show lower reflectances in the forward direction (RAA = 0) as compared to the results from FASMAR and SCIATRAN. The relative difference between FASMAR and SCIATRAN results is within 5 % for typical satellite observation angles. A decrease of BRDF values with increasing wavelength is seen in all three datasets. This feature is caused by the ice crystal absorption.

Further examples of FASMAR and RTLSRS model comparisons with ground-based, aircraft and satellite measurements of snow angular reflectance can be found in Mei et al. (2022).

White ice and snow covered ice

Sea ice is one of the most important surface types in the high latitude ocean regions. Measurements of spectral albedo for typical sea ice conditions were per-

https://doi.org/10.5194/gmd-2022-153
Preprint. Discussion started: 1 July 2022

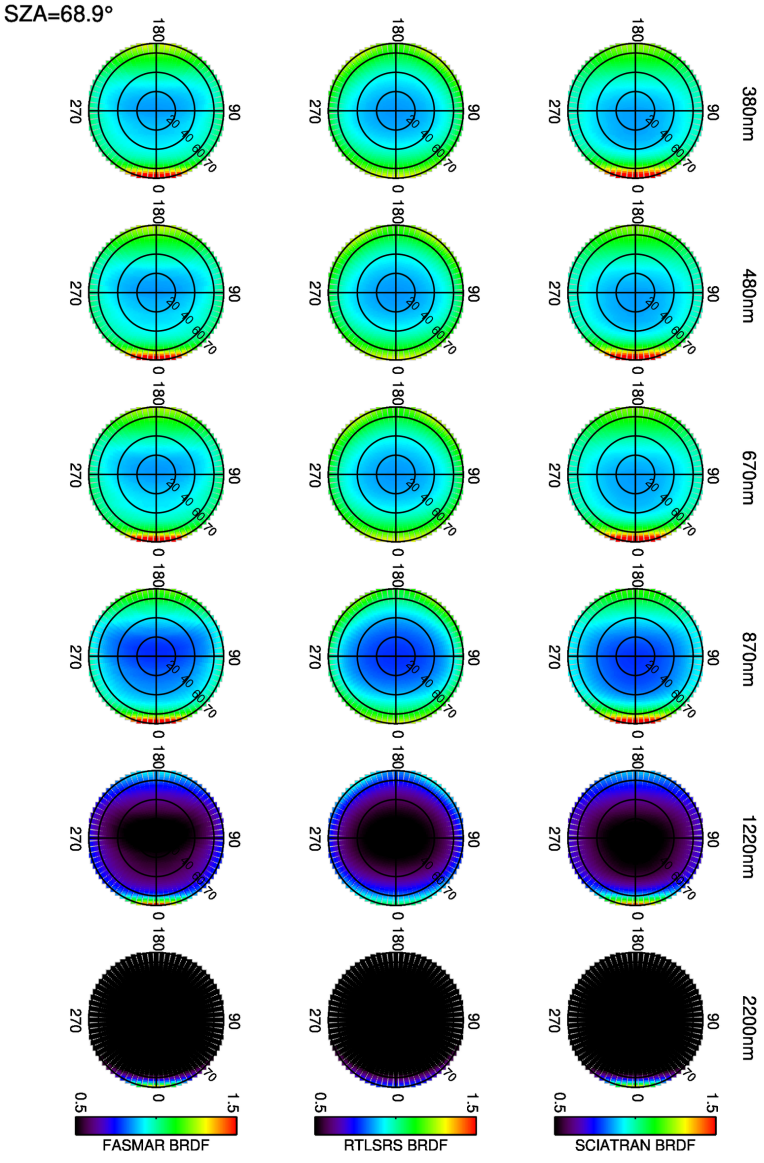

Figure 6: BRDF of the snow layer calculated using SCIATRAN and fitting results using RTLSRS model and FASMAR for wavelengths of 380, 480 , 670 , 870, 1220, and 2200 nm and a solar zenith angle of 68.9°

https://doi.org/10.5194/gmd-2022-153
Preprint. Discussion started: 1 July 2022


Geoscientific Model Development Discussions
Open Access
EGU

formed in the spectral range 350 - 1350 nm during the R/V Polarstern cruise ARK-XXVII/3 from 2 August to 8 October 2012 (Malinka et al., 2016). Two examples of bright white ice spectral albedo measurements, as presented in Malinka et al. (2016) (see their Fig. 8(a) and (c)), are used in this paper as well. The scattering layer for these two examples is about 3 – 8 cm thick while the near surface air temperature is about -1.2 ° C. Such sea ice scenarios represent intermediate phase between a typical snow and white ice (Malinka et al., 2016). Simulations with SCIATRAN were performed using the stochastic model of the surface reflection described in Sect. 4.3.3 and an aerosol-free atmosphere without gaseous absorption. Figures 7(a) and 7(b) show comparisons of measured and modelled bright white ice spectral albedo with and without yellow substance absorption, respectively.

Three parameters required to initialise the BRDF model in SCIATRAN (snow layer optical thickness, mean chord and DOM absorption) were obtained by fitting the simulated albedo with respect to the measured one within the spectral range 350 - 1350 nm. The following parameters provide the minimal residual: (350.0, 510.6 μm, and 0.71 m^{-1}) and (14.1, 776.2 μm, and 0.001 m^{-1}) for Fig. 7(a) and Fig. 7(b), respectively. The spectral behaviour in the visible spectral range determined by the yellow substance absorption is well reproduced by SCIATRAN. The RMSE values between SCIATRAN simulations and measurements are $1.2 \cdot 10^{-2}$ and $1.5 \cdot 10^{-2}$, respectively, confirming a correct implementation of the stochastic model of random mixtures of ice particles and air gaps into SCIATRAN.

Melt ponds on sea ice

Melt ponds on sea ice is another surface type typical for high latitude regions. Comparisons of SCIATRAN simulations for spectral albedo of light-blue and dark open melt ponds with measurement data are shown in Fig. 8. Measurements of spectral albedo were performed in the spectral range 300 - 2500 nm on August 2012 during a Polarstern cruise (Malinka et al., 2018). The examples presented in Fig. 8 were selected following Malinka et al. (2018). The spectral albedo of blue and dark melt ponds was measured under cloud-free and cloudy

https://doi.org/10.5194/gmd-2022-153
Preprint. Discussion started: 1 July 2022

Geoscientific Model Development
Discussions
Open Access
EGU

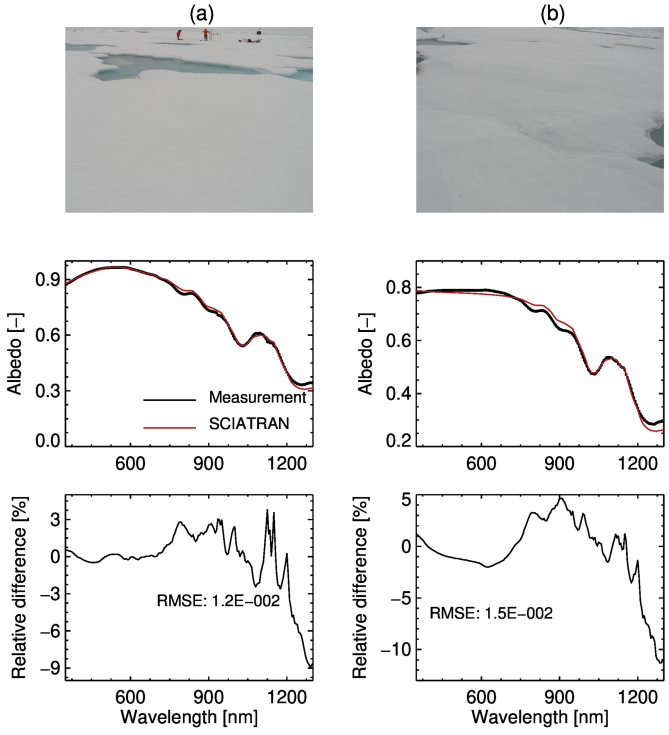

Figure 7: Comparisons of measured and simulated bright white ice spectral albedo corresponding to Figs. 8a and 8c in Malinka et al. (2016). The upper row shows pictures of the measurements conditions, the middle row shows the measured and simulated spectral albedo, and the lower row shows the percentage difference between SCIATRAN simulations and campagin measurements.

https://doi.org/10.5194/gmd-2022-153
Preprint. Discussion started: 1 July 2022


Geoscientific Model Development Discussions
Open Access
EGU

condition, respectively.

The simulations with SCIATRAN were performed using the stochastic model of the surface reflection described in Sect. 4.3.3 and aerosol-free atmosphere without gaseous absorption. The spectral albedo was calculated as a ratio of the reflected to the incident fluxes at the surface. For the blue pond, a cloud-free atmosphere was selected and the solar zenith angle was set in accordance with (Malinka et al., 2018) to 70°. For the dark pond, a water cloud with the optical thickness of 20, the geometrical thickness of 0.5 km, and the top height of 1.5 km was considered in addition.

Three parameters required to initialise the BRDF model in SCIATRAN (ice thickness, water depth and transport scattering coefficient) were obtained by fitting the simulated albedo with respect to the measured one within the spectral range 350 - 1350 nm. As pointed out by Malinka et al. (2018), measurements outside this spectral range show strong noise contamination. Therefore they were not used in the fitting process. The following parameters provide the minimum residual: (281.2 cm, 14.6 cm, and 2.08 m^{-1}) and (23.7 cm, 42.8 cm, and 0.52 m^{-1}) for the light-blue and dark melt ponds, respectively. It is seen from Fig. 8 that both spectral patterns and magnitudes of the spectral albedo agree well between the SCIATRAN simulations and the measurements, especially for for the light-blue melt ponds. As expected, the spectral albedo for the dark melt ponds is significantly lower than that for light-blue ones because of a much larger water depth. Typical spectral features can be seen for both scenes: 1) a higher albedo in the visible range and lower albedo in the infrared range; 2) a weak spectral dependence of the albedo in the NIR range. Both features above can be explained due to the wavelength dependence of water absorption and Fresnel reflection at the air-water interface. Indeed, in contrast to the visible range, water absorbs a significant amount of radiation in the NIR so that a few centimetres thick layer of water completely absorbs radiation. This results in a saturation effect when variation of water absorption coefficient does not lead to the variation of albedo and the wavelength dependence of albedo is mainly caused by spectral dependence of Fresnel reflection.

https://doi.org/10.5194/gmd-2022-153
Preprint. Discussion started: 1 July 2022

Geoscientific Model Development Discussions

The RMSE values between SCIATRAN simulations and measurements are $1.1 \cdot 10^{-2}$ and $3.8 \cdot 10^{-3}$ for the light-blue and dark melt ponds, respectively, confirming a correct implementation of the ice and melt ponds models in SCIATRAN.

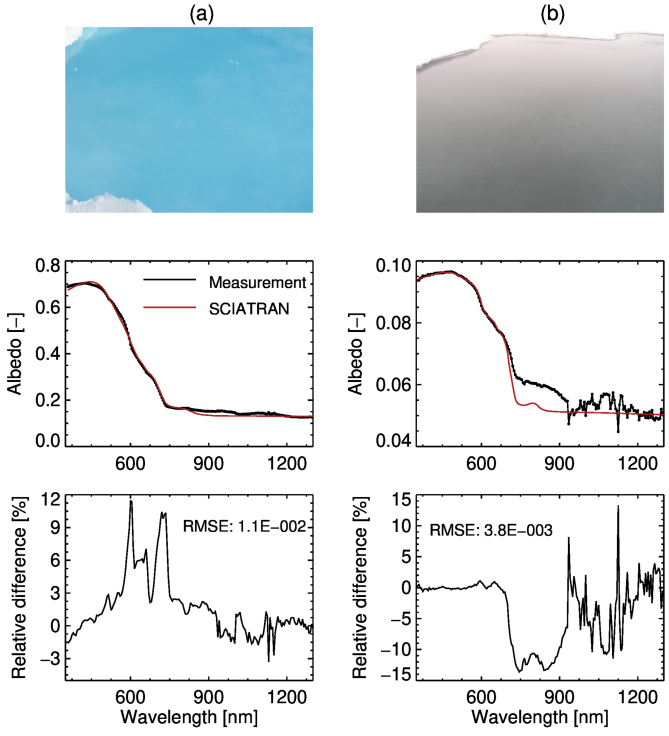

Figure 8: Comparisons of the spectral albedo for the light-blue (a) and dark (b) melt ponds corresponding to Fig. 6a and Fig. 8a in Malinka et al. (2018). The upper row shows pictures of the measurement scenes, the middle row shows the measured and simulated spectral albedo, and the lower row shows relative differences between the SCIATRAN simulations and campagin measurements.

https://doi.org/10.5194/gmd-2022-153
Preprint. Discussion started: 1 July 2022


Geoscientific Model Development Discussions
Open Access
EGU

7. Conclusions

This paper summerizes recent updates and new developments of aerosol, clouds and surface reflectance databases and models in the framework of the software package SCIATRAN. These updates and developments extend the capabilities of the radiative transfer modelling, especially by accounting for different kinds of vertical inhomogeneties. Vertically inhomogeneous ice and mix-phase clouds and different aerosol types can be easily accounted for within SCIATRAN (V4.6). Additionally, widely used models and databases for the surface BRDF and albedo for different surface types (ocean, land, vegetation, snow, and melt pond on sea ice) are available with friendly user-interfaces. We believe that presented updates and new developments largely extend the application range of the SCIATRAN model in the field of the aerosol, cloud and surface remote sensing. The new implementations have been used or been planned for use to support the development and generation of the XBAER global aerosol, cloud and surface data products. Users are advised to use the latest version of SCIATRAN capable of the new features described in this manuscript. The extended SCIATRAN version is freely available for students and scientists affiliated at academic facilities after a registration at the website of IUP, University of Bremen: http://www.iup.physik.uni-bremen.de/sciatran

8. Appendix

8.1. White ice

The analytical expressions for the auxiliary function T_{dif}, average cosine g and absorption coefficient of the yellow substance α_y used in the white ice model described in Sect. 4.3.3 are given below following Malinka (2014, 2015) and Malinka et al. (2016).

https://doi.org/10.5194/gmd-2022-153
Preprint. Discussion started: 1 July 2022

Geoscientific Model Development Discussions
Open Access
EGU

The auxiliary function T_{dif} is defined as

$$T_{dif} = \frac{2(5n^6+8n^5+6n^4-5n^3-n-1)}{3(n^3+n^2+n+1)\,(n^4-1)} + \frac{n^2(n^2-1)^2}{(n^2+1)^3}\,\ln\frac{n+1}{n-1} - \frac{8n^4(n^4+1)}{(n^4-1)^2(n^2+1)}\,\ln n\,. \tag{30}$$

The analytical expression for the average cosine g of the phase function is given by

$$g = \frac{1}{\omega}\left[r_1 + \frac{n^2\,t_1^2}{T_{dif}(1-n^2) - r_1 + n^4(1+\alpha\,a)}\right]\,, \tag{31}$$

where r_1 and t_1 are

$$r_1 = \frac{n(3n^{11}+3n^{10}+25n^9+25n^8+22n^7-282n^6+138n^5+186n^4+151n^3-89n^2+13n-3)}{24(n+1)\,(n^4-1)\,(n^2+1)^2} + \frac{8n^4(n^6-3n^4+n^2-1)}{(n^4-1)^2(n^2+1)^2}\,\ln n - \frac{(n^8+12n^6+54n^4-4n^2+1)(n^2-1)^2}{16(n^2+1)^4}\,\ln\frac{n+1}{n-1}\,, \tag{32}$$

$$t_1 = \frac{3n^8+3n^7-17n^6+55n^5-39n^4-7n^3-27n^2-11n-8}{24(n+1)\,(n^4-1)\,n} - \frac{(n^2-1)^4}{16(n^2+1)^2n}\,\ln\frac{n+1}{n-1} + \frac{4n^5}{(n^4-1)^2}\,\ln n\,. \tag{33}$$

The absorption coefficient of the yellow substance is given by

$$\alpha_y(\lambda) = \begin{cases} \alpha_y(\lambda_0)\,e^{-0.015\,(\lambda-\lambda_0)}\,, & \lambda \le 500\,\mathrm{nm} \\ \alpha_y(\lambda_0)\,e^{-0.015\,(500-\lambda_0)-0.011(\lambda-500)}\,, & \lambda > 500\,\mathrm{nm} \end{cases}\,, \tag{34}$$

where $\lambda_0 = 390\,\mathrm{nm}$ and $\alpha_y(\lambda_0)$ is the absorption coefficient of the yellow substance at the wavelength λ_0.

8.2. Melt ponds

The albedo of the under-pond ice layer needed by the melt pont model described in Sect. 4.3.3 is calculated according to the two-stream approximation developed by Zege et al. (1991):

$$A_b \;=\; A_0\,\frac{1-e^{-2\gamma\tau}}{1-A_0^2\,e^{-2\gamma\tau}}\,, \tag{35}$$

https://doi.org/10.5194/gmd-2022-153
Preprint. Discussion started: 1 July 2022

Geoscientific Model Development Discussions
Open Access
EGU

where $A_0 = 1 + t - \sqrt{t\,(t+2)}$ is the albedo of the semi-infinite layer with the same optical characteristics, $t = 8\,\alpha_i / 3\,\sigma_t$, $\tau = (\sigma_t + \alpha_i)\,H$ is the layer optical thickness, H is its geometrical thickness, and γ is the asymptotic attenuation coefficient given by

$$\gamma = \frac{3}{4}\,\frac{\sigma_t}{\sigma_t + \alpha_i}\sqrt{t\,(t+2)}\,. \tag{36}$$

Here, α_i and σ_t are the ice absorption coefficient and transport scattering coefficient of ice (see e.g. Chandrasekhar (1950)), respectively.

9. Code and data availability

The SCIATRAN software package and database are available at http://www.iup.physik.uni-bremen.de/sciatran

10. Author contribution

LM and VR designed the experiments, LM, VR and AR developed the model code and performed the simulations. LM and VR prepared the manuscript with contributions from all co-authors. JB provided general oversight and guidance.

11. Competing interests

The contact author has declared that neither he nor the co-authors have any competing interests.

https://doi.org/10.5194/gmd-2022-153
Preprint. Discussion started: 1 July 2022

12. Acknowledgments

The valueable discussions with Dr. Robert Levy, Dr. Peter Colarco, Dr. Ping Yang, Dr. Bryan A. Baum, Dr. Masanori Saito, Dr. Oleg Dubovik and Dr. Aleksey Malinka are highly appreciated.

13. Financial support

This research was funded by the Deutsche Forschungsgemeinschaft (DFG, German Research Foundation) – Project-ID 268020496 – TRR 172.

https://doi.org/10.5194/gmd-2022-153
Preprint. Discussion started: 1 July 2022

Geoscientific Model Development Discussions

References

C. Arosio, A. Rozanov, E. Malinina, K.-U. Eichmann, T. von Clarmann, and J. P. Burrows. Retrieval of ozone profiles from OMPS limb scattering observations. *Atmospheric Measurement Techniques*, 11(4):2135–2149, 2018. doi: 10.5194/amt-11-2135-2018. URL `https://amt.copernicus.org/articles/11/2135/2018/`.

B.A. Baum, P. Yang, A.J. Heymsfield, S. Platnick, M.D. King, and S.T. Bedka. Bulk scattering models for the remote sensing of ice clouds Part II: Narrowband models. *J. Appl. Meteor.*, 44:1896–1911, 2005.

B.A. Baum, P. Yang, A.J. Heymsfield, C.G. Schmitt, Y. Xie, and A. Bansemer. Improvements in shortwave bulk scattering and absorption models for the remote sensing of ice clouds. *J. Appl. Meteorol. Climatol.*, 50:1037 – 1056, 2011.

H.J. Bolle. A preliminary cloudless stardard atmosphere for radiation computation, wcp-112. *World Meteorological Organization*, 1986.

H. Bovensmann, M. Buchwitz, J. P. Burrows, M. Reuter, T. Krings, K. Gerilowski, O. Schneising, J. Heymann, A. Tretner, and J. Erzinger. A remote sensing technique for global monitoring of power plant CO_2 emissions from space and related applications. *Atmospheric Measurement Techniques*, 3(4):781–811, 2010. doi: 10.5194/amt-3-781-2010. URL `https://amt.copernicus.org/articles/3/781/2010/`.

F.M. Breon and E. Vermote. Correction of MODIS surface reflectance time series for BRDF effects. *Remote Sensing of Environment*, 125:1–9, 2012.

M. Buchwitz, M. Reuter, H. Bovensmann, D. Pillai, J. Heymann, O. Schneising, V. Rozanov, T. Krings, J. P. Burrows, H. Boesch, C. Gerbig, Y. Meijer, and A. Löscher. Carbon monitoring satellite (CarbonSat): assessment of atmospheric CO_2 and CH_4 retrieval errors by error parameterization. *Atmospheric Measurement Techniques*, 6(12):3477–3500, 2013. doi:

https://doi.org/10.5194/gmd-2022-153
Preprint. Discussion started: 1 July 2022

10.5194/amt-6-3477-2013. URL https://amt.copernicus.org/articles/6/3477/2013/.

J. P. Burrows, E. Holzle, A. P. H. Goede, H. Visser, and W. Fricke. Sciamachy - scanning imaging absorption spectrometer for atmospheric chartography. *Acta Astronautica*, 35(7):445–451, 1995.

S. Chandrasekhar. *Radiative transfer*. London: Oxford University Press, 1950.

M. Degunther and R. Meerkotter. Influence of inhomogeneous surface albedo on uv irradiance: effect of a stratus cloud. *Journal of Geophysical Research*, 105:D18, 2000.

O. Dubovik, A. Sinyuk, T. Lapyonok, B. N. Holben, M. Mischchenko, P. Yang, T. F. Eck, H. Volten, O. Munoz, B. Veihelmann, W. J. van der Zande, J. F. Leon, M. Sorokin, and I. Slutsker. Application of spheroid models to account for aerosol particle nonsphericity in remote sensing of desert dust. *Journal of Geophysical Rsearch : Atmospheres*, 111:D11, 2006.

O. Dubovik, T. Lapyonok, P. Litvinov, M. Herman, D. Fuertes, F. Ducos, A. Lopatin, A. Chaikovksy, B. Torres, Y. Derimain, X. Huang, M. Aspetsberger, and C. Federspiel. Grasp: a versatile algorithm for characterizing the atmosphere. *SPIE News-room*, 2014. doi: 10.1117/2.1201408.005558.

E. M. Feigelson, editor. *Radiation in cloudy atmosphere*. Gidrometeoizdat (in Russian), Leningrad, 1981.

K. Gerilowski, A. Tretner, T. Krings, M. Buchwitz, P. P. Bertagnolio, F. Belemezov, J. Erzinger, J. P. Burrows, and H. Bovensmann. Mamap – a new spectrometer system for column-averaged methane and carbon dioxide observations from aircraft: instrument description and performance analysis. *Atmos. Meas. Tech.*, 4:215–243, 2011.

M. Hess, P. Köpke, and I. Schult. Optical properties of aerosols and clouds: The software package OPAC. *Bulletin of the American Meteorological Socie*, 79:831–844, 1998.

https://doi.org/10.5194/gmd-2022-153
Preprint. Discussion started: 1 July 2022

S. Jacquemound, W. Verhoef, F. Baret, C. Bacour, P.J. Zarco-Tejade, G. P. Asner, C. Francois, and S. L. Ustin. Prospect + sail models : A review of use for vegetation characterization. *Remote sensing of environment*, 113:S56 – S66, 2009.

E. Jarvinen, E. Jourdan, D. Neubauer, B. Yao, C. Liu, M.O. Andreae, U. Lohmann, M. Wendisch, G. M. McFarquhar, T. Leisner, and M. Schnaiter. Additional global climate colling by clouds due to ice crystal complexity. *Atmospheric Chemistry and Physics*, 18:15767 – 15781, 2018.

Z.T. Jiao, A Ding, A. Kokhanvosky, C. Schaaf, F.-M. Bréon, Y. Dong, Z. Wang, Y. Liu, X. Zhang, S. Yin, L. Cui, L. Mei, and Y. Chang. Development of a snow kernel to better model the anisotropic reflectance of pure snow in a kernel-driven BRDF model framework. *Remote Sensing of Environment*, 221: 198–209, 2019.

M.D. King, S. Platnick, W.P. Menzel, S.A. Ackerman, and P.A. Hubanks. Spatial and temporal distribution of clouds observed by modis onboard the terra and aqua satellites. *IEEE Transactions on Geoscience and Remote Sensing*, 51:3826 – 3852, 2013.

A. A. Kokhanovsky. Reflection of light from particulate media with irregularly shaped particles. *Journal of Quantitative Spectroscopy and Radiative Transfer*, 96:1–10, 2005.

A. A. Kokhanovsky and V. V. Rozanov. Droplet vertical sizing in warm clouds using passive optical measurements from a satellite. *Atmos. Meas. Tech.*, 5 (3):517–528, 2012.

A. A. Kokhanovsky and E. P. Zege. Scattering optics of snow. *Applied Optics*, 43:1589–1602, 2004.

P. Köpke, J. Gasteiger, and M. Hess. Technical Note: Optical properties of desert aerosol with non-spherical mineral particles: data incorporated to OPAC. *Atmos. Chem. Phys.*, 15:5947–5956, 2015.

https://doi.org/10.5194/gmd-2022-153
Preprint. Discussion started: 1 July 2022

L. Lelli, V. V. Rozanov, M. Vountas, and J. P. Burrows. Polarized radiative transfer through terrestrial atmosphere accounting for rotational raman scattering. *Journal of Quantitative Spectroscopy and Radiative Transfer*, 200: 70–89, 2017.

C. Levoni, M. Cervino, R. Guzzi, and F. Torricella. Atmospheric aerosol optical properties: a database of radiative characteristics for different components and classes. *Apppl. Opt.*, 36:8031 – 8041, 1997.

R. C. Levy, L. A. Remer, and O. Dubovik. Global aerosol optical properties and application to Moderate Resolution Imaging Spectroradiometer aerosol retrieval over land. *Journal of Geophysical Research*, 112:D13210, 2007.

R. C. Levy, S. Mattoo, L. A. Munchak, L. A. Remer, A. M. Sayer, F. Patadia, and N. C. Hsu. The collection 6 modis aerosol products over land and ocean. *Atmospheric Measurement Techniques*, 6:2989–3034, 2013.

W. Lucht, C. B. Schaaf, and A. H. Strahler. An algorithm for the retrieval of albedo from space using semiempirical BRDF models. *IEEE TRANSACTIONS ON GEOSCIENCE AND REMOTE SENSING*, 38:977–998, 2000.

A. Macke, J. Mueller, and E. Raschke. Scattering properties of atmospheric ice crystals. *J. Atmos. Sci.*, 53:2813–25, 1996.

F. Maignan, F. M. Breon, and R. Lacaze. Bidirectional refletance of earth targets: evaluation of analytical models using a large set of space-borne measurements with emphasis on the hot spot. *Remote Sensing of Environment*, 90:210–20, 2004.

A. Malinka. Analytical expressions for characteristics of light scattering by arbitrarily shaped particles in the wkb approximation. *J. Opt. Soc. Am. A*, 32:1344–1351, 2015.

A. Malinka, E. Zege, G. Heygster, and L. Istomina. Reflective properties of white sea ice and snow. *The Cryosphere*, 10:2541–2557, 2016. doi: https://doi.org/10.5194/tc-10-2541-2016.

https://doi.org/10.5194/gmd-2022-153
Preprint. Discussion started: 1 July 2022

A. Malinka, E. Zege, L. Istomina, G. Heygster, G. Spreen, D. Perovich, and C. Polashenski. Reflective properties of melt ponds on sea ice. *The Cryosphere*, 12:1921 – 1937, 2018.

A. V. Malinka. Light scattering in porous materials: Geometrical optics and stereological approach. *Journal of Quantitative Spectroscopy and Radiative Transfer*, 141:14–23, 2014.

E. Matthews. Global vegetation and land use: new high resolution databases for climate studies. *J. Clim. Appl. Meteorol.*, 22:474–87, 1983.

L. Mei, V. Rozanov, M. Vountas, J. P. Burrows, R. C. Levy, and W. Lotz. Retrieval of aerosol optical properties using MERIS observations: Algorithm and some first results. *Remote Sensing of Environment*, 197:125–140, 2017a.

L. Mei, M. Vountas, L. Gómez-Chova, V. Rozanov, M. Jäger, W. Lotz, J.P. Burrows, and R. Hollmann. A cloud masking algorithm for the XBAER aerosol retrieval using MERIS data. *Remote Sensing of Environment*, 197: 141–160, 2017b.

L. Mei, V. Rozanov, M. Vountas, and J.P. Burrows. The retrieval of ice cloud parameters from multi-spectral satellite observations of reflectance using a modified XBAER algorithm. *Remote Sensing of Environment*, 215:128–144, 2018a.

L. Mei, V. Rozanov, M. Vountas, J.P. Burrows, and A. Richter. Xbaer-derived aerosol optical thickness from olci/sentinel-3 observation. *Atmospheric Chemistry and Physics*, 18:2511–2523, 2018b.

L. Mei, V. Rozanov, H. Jethva, K. G Meyer, L. Lelli, M. Vountas, and J.P. Burrows. Extending xbaer algorithm to aerosol and cloud condition. *IEEE Transactions on Geoscience and Remote Sensing*, 57:1–14, 2019.

L. Mei, S. Vandenbussche, V. Rozanov, E. Proestakis, V. Amiridis, S. Callewaert, M. Vountas, and J.P. Burrows. On the retrieval of aerosol optical

https://doi.org/10.5194/gmd-2022-153
Preprint. Discussion started: 1 July 2022

depth over cryosphere using passive remote sensing. *Remote sensing of Environment*, 241:111731, 2020a.

L. Mei, V. Rozanov, C. Ritter, B. Heinold, Z. Jiao, M. Vountas, and J. P. Burrows. Retrieval of aerosol optical thickness in the Arctic snow-covered regions using passive remote sensing: Impact of aerosol typing and surface reflection model. *IEEE Transactions on Geoscience and Remote Sensing*, 58: 5117–5131, 2020b.

L. Mei, V. Rozanov, C. Pohl, M. Vountas, and J. P. Burrows. The retrieval of snow properties from SLSTR/Sentinel-3 – part 1: method description and sensitivity study. *The Cryosphere*, pages 1–45, 2021a. doi: 10.5194/tc-2020-269. URL `https://tc.copernicus.org/preprints/tc-2020-269/`.

L. Mei, V. Rozanov, E. Jäkel, X. Cheng, M. Vountas, and J. P. Burrows. The retreival of snow properties from SLSTR/Sentinel-3 – part 2: results and validation. *The Cryosphere*, pages 1–41, 2021b. doi: 10.5194/tc-2020-270. URL `https://tc.copernicus.org/preprints/tc-2020-270/`.

L. Mei, V. Rozanov, Z. Jiao, and J. P. Burrows. A new snow bidirectional reflectance distribution function model in spectral regions from UV to SWIR: model development and application to ground-based, aircraft and satellite observations. *ISPRS Journal of Photogrammetry and Remote Sensing*, 188: 269–285, 2022.

M. I. Mishchenko. Radiation force caused by scattering, absorption, and emission of light by nonspherical particles. *Journal of quantitative spectroscopy and radiative transfer*, 70:811 – 816, 2001.

M.I. Mishchenko, J. M. Dlugach, E.G. Yanvitskij, and N. T. Zakharova. Bidirectional reflectance of flat, optically thick particulate layers: an efficient radiative transfer solution and applications to snow and soil surface. *Journal of quantitative spectroscopy and radiative transfer*, 63:409 – 432, 1999.

https://doi.org/10.5194/gmd-2022-153
Preprint. Discussion started: 1 July 2022


Geoscientific Model Development Discussions

S. Noël, K. Weigel, K. Bramstedt, A. Rozanov, M. Weber, H. Bovensmann, and J. P. Burrows. Water vapour and methane coupling in the stratosphere observed using SCIAMACHY solar occultation measurements. *Atmospheric Chemistry and Physics*, 18(7):4463–4476, 2018. doi: 10.5194/acp-18-4463-2018. URL https://acp.copernicus.org/articles/18/4463/2018/.

S. Platnick, K. G. Meyer, M. D. King, G. Wind, N. Amarasinghe, B. Marchant, G. T. Arnold, Z. Zhang, P. A. Hubanks, R.E. Holz, P. Yang, W. L. Ridgway, and J. Riedi. The modis cloud optical and mircophysical products: Collection 6 updates and examples from terra and aqua. *IEEE Trans. Geosci. Remote Sens.*, 55:502 – 525, 2017.

C. Pohl, V. V. Rozanov, L. Mei, J. P. Burrows, G. Heygster, and G. Spreen. Implementation of an ice crystal single-scattering property database in the radiative transfer model SCIATRAN. *Journal of Quantitative Spectroscopy and Radiative Transfer*, 253:107118, 2020.

H. Rahman, B. Pinty, and M.M. Verstraete. Coupled surface-atmosphere reflectance (CSAR) model 2. Semiempirical surface model usable with NOAA advanced very high resolution radiometer data. *Journal of Geophysical Research*, 98:20791–20801, 1993.

C.A. Randles, A.M. da Silva, P. R. Colarco V. Buchard, A. Darmenov, R. Govindaraju, A. Smirnov, B. Holben, R. Ferrare, J. Hair, Y. Shinozuka, and C. J. Flynn. The merra-2 aerosol reanalysis, 1980 onward. part 1: System description and data assimilation evaluation. *Journal of Climate*, 30:6823 – 6850, 2017.

L. A. Remer, Y.J. Kufman, D. Tanre, S. Mattoo, D.A. Chu, J.V. Martins, R.R. Li, C. Ichoku, R.C. Levy, R.G. Kleidman, T.F. Eck, E. Vermote, and B.N. Holben. The MODIS aerosol algorithm, products and validation. *Journal of the atmospheric sciences*, 62:947–973, 2005.

https://doi.org/10.5194/gmd-2022-153
Preprint. Discussion started: 1 July 2022

L. A. Remer, R.C. Levy, S. Mattoo, D. Tanre, P. Gupta, Y. Shi, V. Sawyer, L. A. Munchak, Y. P. Zhou, M. Kim, C. Ichoku, F. Patadia, R. R. Li, S. Gasso, R. G. Kleidman, and B. N. Holben. The dark target algorithm for observing the global aerosol system: Past, present , and future. *Remote sensing*, 12: 2900, 2020.

M. Reuter, M. Buchwitz, O. Schneising, S. Noël, V. Rozanov, H. Bovensmann, and J.P. Burrows. A fast atmospheric trace gas retrieval for hyperspectral instruments approximating multiple scattering—part 1: Radiative transfer and a potential oco-2 xco2 retrieval setup. *Remote Sens.*, 9:1159, 2017.

A. Richter, J.P. Burrows, H. Nuess, C. Granier, and U. Niemeier. Increase in tropospheric nitrogen dioxide over China observed from space. *Nature*, 437: 129–132, 2005.

J. L. Roujean, M. Leroy, and P. Y. Deschamps. A bidirectional reflectance model of the Earth's surface for the correction of remote sensing data. *J. Geophys. Res. Atmos.*, 97:20455–20468, 1992.

A. Rozanov, V. V. Rozanov, M. Buchwitz, A. Kokhanovsky, and J. P. Burrows. Sciatran 2 - a new radiative transfer model for geophysical applications in the 175 - 2400 nm spectral region: the pseudo-spherical version. *Adv. Space Res.*, 36:1015–9, 2005.

A. Rozanov, V. V. Rozanov, and J. P. Burrows. Modeling of inelastically scattered radiation: Rotational raman scattering in the spherical earth's atmosphere. *Journal of Quantitative Spectroscopy and Radiative Transfer*, 268: 107611, 2021.

V. V. Rozanov and M. Vountas. Radiative transfer equation accounting for rotational raman scattering and its solution by the discrete-ordinates method. *Journal of Quantitative Spectroscopy and Radiative Transfer*, 133:603–618, 2013.

https://doi.org/10.5194/gmd-2022-153
Preprint. Discussion started: 1 July 2022

V. V. Rozanov, D. Diebel, R.J.D. Spurr, and J. P. Burrows. Gometran: a radiative transfer model for the satellite project gome, the plane-parallel version. *J. Geophys. Res.*, 102:16683–95, 1997.

V. V. Rozanov, M. Buchwitz, K.-U. Eichmann, R. de Beek, and J. P. Burrows. Sciatran - a new radiative transfer model for geophysical applications in the 240 - 2400 nm spectral region: the pseudo-spherical version. *Adv. Space Res.*, 29:1831–5, 2002.

V. V. Rozanov, A. V. Rozanov, A. A. Kokhanovsky, and J. P. Burrows. Radiative transfer through terrestrial atmosphere and ocean: software package SCIATRAN. *J. Quant. Spectr. Radiat. Transfer*, 133:13–71, 2014. doi: 10.1016/j.jqsrt.2013.07.004.

V. V. Rozanov, T. Dinter, A. V. Rozanov, A. Wolanin, A. Bracher, and J. P. Burrows. Radiative transfer modeling through terrestrial atmosphere and ocean accounting for inelastic processes: Software package SCIATRAN. *Journal of Quantitative Spectroscopy and Radiative Transfer*, 194:65–85, 2017.

M. Saito, P. Yang, N. G. Loeb, and S. Kato. A novel parameterization of snow albedo based on a two-layer snow model with a mixture of grain habits. *J. Atmos. Sci.*, 76:1419–1436, 2019.

D. Segelstein. The complex refractive index of water. *Master thesis*, University of Missouri, 1981.

B. M. Sinnhuber, N. Sheode, M. Sinnhuber, M.P. Chipperfield, and W. Feng. The contribution of anthropogenic bromine emissions to past stratospheric ozone trends: a modelling study. *Atmos. Chem. Phys.*, 9:2863 – 2871, 2009.

A. Smirnov, B.N. Holben, I. Slutsker, D. M. Giles, C. R McClain, T. F. Eck, S. M. Sakerin, A. Macke, P. Croot, G. Zibordi, P. K. Quinn, J. Sciare, S. Kinne, M. Harvey, T. J. Smyth, S. Piketh, T. Zielinkski, A. Proshutinsky, J. I. Goes, N. B. Nelson, P. Larouche, V. F. Radionov, P. Goloub, K. Krishna Moorthy, R. Matarrese, E. J. Robertson, and F. Jourdin. Maritime aerosol

https://doi.org/10.5194/gmd-2022-153
Preprint. Discussion started: 1 July 2022


Geoscientific Model Development Discussions

network as a component of aerosol robotic network. *Journal of Geophysical Research*, 114:D06204, 2009.

V. V. Sobolev. *Light Scattering in Planetary Atmospheres*. Nauka, Moscow, 1972.

E. Vermote, C. O. Justice, and F.-M. Bréon. Towards a generalized approach for correction of the BRDF effect in MODIS directional reflectances. *IEEE TRANSACTIONS ON GEOSCIENCE AND REMOTE SENSING*, 47:898–908, 2009.

M. Weber, M. Coldewey-Egbers, V. E. Fioletov, S. M. Frith, J. D. Wild, J. P. Burrows, C. S. Long, and D. Loyola. Total ozone trends from 1979 to 2016 derived from five merged observational datasets – the emergence into ozone recovery. *Atmospheric Chemistry and Physics*, 18(3):2097–2117, 2018. doi: 10.5194/acp-18-2097-2018. URL `https://acp.copernicus.org/articles/18/2097/2018/`.

A. Wolanin, V. V. Rozanov, T. Dinter, S. Noël, M. Vountas, J. P. Burrows, and A. Bracher. Global retrieval of marine and terrestrial chlorophyll fluorescence at its red peak using hyperspectral top of atmosphere radiance measurements: Feasibility study and first results. *Remote Sensing of Environment*, 166:243 – 261, 2015.

P. Yang, L. Bi, B. A. Baum, K-N. Liou, G.W. Kattawar, M.I. Mishchenko, and B. Cole. Spectrally consistent scattering, absorption, and polarization properties of atmospheric ice crystals at wavelengths from 200 to 100000 nm. *Journal ofAtmospheric Sciences*, 70:330–347, 2013.

E. P. Zege, A. P. Ivanov, and I. L. Katsev. Image transfer through a scattering medium. *Springer-Verlag Berli Heidelberg*, 1:349, 1991.

T. X. P. Zhao, I. Laszlo, O. Dubovik, B. N. Holben, J. Sapper, D. tanre, and C. pietras. A study of the effect of non-spherical dust particles on the avhrr

https://doi.org/10.5194/gmd-2022-153
Preprint. Discussion started: 1 July 2022

aerosol optical thickness retrievals. *Journal of quantitative spectroscopy and radiative transfer*, 30:1317, 2003.